Author/s:
Ganio, K;Nasreen, M;Yang, Z;Maunders, EA;Luo, Z;Hossain, SI;Ngu, DHY;Ellis, D;Gu, J;Neville, SL;Wilksch, J;Gunn, AP;Whittall, JJ;Kobe, B;Deplazes, E;Kappler, U;McDevitt, CA

Title:
Hfe Permease and Haemophilus influenzae Manganese Homeostasis

Date:
2024-01-19

Citation:
Ganio, K., Nasreen, M., Yang, Z., Maunders, E. A., Luo, Z., Hossain, S. I., Ngu, D. H. Y., Ellis, D., Gu, J., Neville, S. L., Wilksch, J., Gunn, A. P., Whittall, J. J., Kobe, B., Deplazes, E., Kappler, U. & McDevitt, C. A. (2024). Hfe Permease and Haemophilus influenzae Manganese Homeostasis. ACS Infectious Diseases, 10 (2), pp.436-452. https://doi.org/10.1021/acsinfecdis.3c00407.

Persistent Link:
https://hdl.handle.net/11343/340388

The Hfe permease and *Haemophilus influenzae* manganese homeostasis

Katherine Ganio[a], Marufa Nasreen[b,c], Zihao Yang[b,c], Eve A. Maunders[a], Zhenyao Luo[b,c,d], Sheikh Imamul Hossain[b,e], Dalton H.Y Ngu[b,c,d], Daniel Ellis[b,c], Jin Gu[b,c], Stephanie L. Neville[a], Jonathan Wilksch[a], Adam P. Gunn[a], Jonathan J. Whittall[f], Boštjan Kobe[b,c,d], Evelyne Deplazes[b,e], Ulrike Kappler[b,c,*], Christopher A. McDevitt[a,*]

[a] Department of Microbiology and Immunology, The Peter Doherty Institute for Infection and Immunity, The University of Melbourne, Melbourne, Victoria, 3000, Australia

[b] School of Chemistry and Molecular Biosciences, The University of Queensland, St Lucia, Queensland, 4072, Australia

[c] Australian Infectious Diseases Research Centre, The University of Queensland, St Lucia, Queensland, 4072 Australia

[d] Institute for Molecular Bioscience, The University of Queensland, St Lucia, Queensland, 4072, Australia

[e] School of Life Sciences, University of Technology Sydney, Ultimo, New South Wales, 2007, Australia

[f] School of Biological Sciences, University of Adelaide, Adelaide, South Australia, 5005, Australia

* Corresponding authors: Ulrike Kappler, E-mail: u.kappler1@uq.edu.au; Christopher A. McDevitt, E-mail: christopher.mcdevitt@unimelb.edu.au

ABSTRACT

Haemophilus influenzae is a commensal of the human upper respiratory tract that can infect diverse host niches due, at least in part, to its ability to withstand both endogenous and host-mediated oxidative stresses. Here we show that *hfeA*, a gene previously linked to iron import, is essential for *H. influenzae* manganese recruitment via the HfeBCD transporter. Structural analyses show that metal-binding in HfeA uses a unique mechanism that involves substantial rotation of the C-terminal lobe of the protein. Disruption of *hfeA* reduces *H. influenzae* manganese acquisition and was associated with decreased growth under aerobic conditions, impaired manganese-superoxide dismutase activity, reduced survival in macrophages, and changes in biofilm production in the presence of superoxide. Collectively, this work shows that HfeA contributes to *H. influenzae* manganese acquisition and virulence attributes. High conservation of the *hfeABCD* permease in *Haemophilus* species suggests that it may serve similar roles in other pathogenic Pasteurellaceae.

Keywords: *Haemophilus influenzae*, Hi2019, metal homeostasis, solute-binding protein, SBP, ABC transporter, host-pathogen, superoxide dismutase

Haemophilus influenzae is a human-adapted respiratory pathogen that commonly inhabits the nasopharynx [1]. From the nasopharynx, *H. influenzae* can disseminate to other parts of the respiratory tract, where it causes acute diseases such as otitis media and pneumonia. *H. influenzae* is also prevalent in exacerbations of multifactorial, chronic respiratory conditions ranging from asthma, chronic obstructive pulmonary disease (COPD), cystic fibrosis, and recovery from SARS-CoV-2 (COVID-19) infections [1-3]. Although a vaccine for *H. influenzae* type B strains is used in many countries, non-typeable *H. influenzae* strains are increasingly prevalent in clinical settings against which the vaccine is not protective [1, 4]. In addition to vaccine escape, non-typeable *H. influenzae* strains also frequently show higher rates of antibiotic resistance and are associated with increased disease severity. These issues have led to *H. influenzae* being listed as a WHO priority pathogen for immediate further action [5].

H. influenzae respiratory tract infections have high rates of recurrence and cause substantial inflammation in the affected areas [1]. These sites of inflammation are enriched for host-produced antibacterial agents that include hydrogen peroxide (H_2O_2) and other reactive oxygen species (ROS). Accordingly, respiratory pathogens have evolved multiple mechanisms to resist oxidative stresses. Studies investigating *H. influenzae* oxidative stress resistance have identified numerous enzymes that contribute to protection that include catalase (*hktE*) and peroxiredoxin (*pgdX*), which degrade H_2O_2 and alkyl hydroperoxides; the DNA-binding ferritin-like protein (*dps*); three periplasmic methionine sulfoxide reductases (*torZ*, *msrAB, dmsABC*); and a manganese (Mn) superoxide dismutase (*sodA*) [6-10]. In addition, key regulators that control responses to oxidative stress have also been identified that include those for H_2O_2 exposure (OxyR), perturbation of iron (Fe) homeostasis (Fur, ferric uptake regulator), and reactive chlorine species induced stress, such as HOCl (RpoE2, alternative sigma factor RpoE2) [11-13]. Nevertheless, there remain unexplored aspects of *H. influenzae* oxidative stress tolerance such as Mn homeostasis, which has a prominent contribution to bacterial stress responses and has recently been shown to have important roles in *H. influenzae* [14-15].

The *d*-block element Mn is an essential metal for all forms of life. In biological systems, Mn can serve in structural and/or catalytic roles within proteins, such as Mn-superoxide dismutase that catalyzes the disproportionation superoxide into H_2O_2 and molecular oxygen and contributes to defense against endogenous and host-mediated oxidative stress. In bacteria, Mn is predominantly acquired by an ATP-binding cassette (ABC) transporter, which belongs to the ABC-3 transport family (Pfam v33.1 identifier PF00950), in conjunction with a solute-binding protein (SBP) that recruits metal ligands from the extra-cytoplasmic space [16]. Mn-specific SBPs belong to the cluster A-I subgroup of ABC transporter-associated SBPs and have a structure defined by a two-lobed organization with N- and C-terminal $(\beta/\alpha)_4$ domains bisected by a cleft within the protein surface in which the ligand binds [17]. Recent studies have shown that despite sharing a similar architecture, the metal-recruiting mechanisms of cluster A-I SBPs have considerable diversity [17-21]. The essentiality of Mn in many bacterial pathogens renders uptake of the metal crucial for infection, with loss of acquisition characterized by a reduction or abrogation of virulence [15, 22-23]. While this is frequently associated with impaired tolerance to oxidative stress, Mn also serves as a cofactor in enzymes involved in primary metabolism, capsule production, and DNA synthesis [24].

Here, we investigate the HfeABCD Mn acquisition pathway of *H. influenzae* 2019 (Hi2019), a strain representative of lower respiratory tract infections, and characterize the genomic, structural, and biochemical properties of the Mn-recruiting SBP, HfeA. Structural and molecular dynamics analyses of HfeA revealed that metal-binding induces conformational changes within the protein that involve partial hinge-bending of the interdomain helix and rotation of the C-terminal domain towards the metal-binding site. Comparisons of *hfeABCD* nucleotide and translated sequences determined that the ABC permease was highly conserved in *H. influenzae* strains and diverse *Haemophilus* species, highlighting the importance of Mn acquisition. Loss of HfeA compromised bacterial Mn uptake, resulting in impaired resistance to superoxide and survival within phagocytic cells. These findings

advance our knowledge of *H. influenzae* Mn homeostasis and highlight the potential contribution of this process to colonization and/or virulence.

RESULTS AND DISCUSSION

Haemophilus influenzae Hi2019 accumulates manganese during growth

The requirement of Hi2019 for Mn was first investigated using different nutritional parameters. Cellular accumulation of the *d*-block elements Mn, iron (Fe), nickel (Ni), cobalt (Co) and zinc (Zn) were assessed in a Mn-limited chemically defined growth medium (CDM), and BHI, a Mn-replete complex, undefined medium (**Table S1**). Hi2019 was grown in CDM or BHI at 37 °C under aerobic conditions, with cultures harvested in mid-exponential phase and metal levels determined (**Fig. 1A**). Despite the ~15-fold difference in ^{55}Mn abundance between the two media (**Table S1**), cellular accumulation of the metal by Hi2019 did not significantly differ between the two media (**Fig. 1A**). Cellular accumulation was also similar for ^{60}Ni and ^{66}Zn in the two nutritional conditions for Hi2019, although ^{56}Fe and ^{59}Co had significantly reduced, ~1.5-fold difference, accumulation in CDM relative to BHI grown cultures (**Fig. 1A**). As total Fe abundance was similar in both media, this may reflect distinct nutritional dependencies associated with the growth profiles in the two types of media or differences in the bioavailability of the metal. By contrast, Co levels were ~21-fold lower in CDM relative to BHI, and the lower abundance may be influencing uptake (**Table S1**). Thus, these data indicate that Hi2019 actively imports Mn and other essential *d*-block elements to achieve specific cellular setpoints.

Recent studies of bacterial Mn homeostasis have shown that intoxication by this element can perturb cell viability due to impacts such as dysregulation of iron homeostasis pathways and impairment of iron-sulfur cluster biogenesis in diverse bacteria [25-26]. Building on the observation that Hi2019 appears to actively import Mn, the impact of elevated Mn concentrations on cell viability was investigated. Titrations with $MnSO_4$ (0 – 10 mM) in BHI had no significant impact on Hi2019 viability except at 10 mM, which showed a modest reduction in viability (**Fig. 1B**). By contrast, Mn supplementation of CDM significantly reduced cell viability at 2.5, 5, and 7 mM $MnSO_4$, with growth completely abrogated at 10 mM $MnSO_4$ (**Fig. 1B**). This difference in cell viability is most likely due

to the distinct composition of the growth media and the presence of Mn-buffering molecules in BHI. Taken together, these data show that Hi2019 can tolerate exposure to supra-physiological Mn concentrations, although viability is perturbed at very high concentrations. We next sought to investigate the mechanistic basis for Hi2019 Mn uptake.

H. influenzae encodes an ABC-3 transport family Mn importer

A bioinformatic approach was used to identify putative Hi2019 Mn uptake pathway(s). Here, the genome was screened for the presence of ABC permeases, natural resistance-associated macrophage proteins (NRAMPs), and P-type ATPases, that have been shown to serve as Mn importers in other bacterial species [27] (**Table S2**). This revealed that the genome of Hi2019 did not encode proteins with substantial similarity (≥ 40% pairwise identity and ≥ 40% query cover) to known Mn-transporting NRAMPs or P-type ATPases. By contrast, Hi2019 encoded a metal ABC transporter solute-binding protein (SBP; C645_RS02315; WP_005656358.1) with similarity to two SBPs associated with ABC permease-dependent Mn import (**Table S2**), YfeA, from *Yersinia pestis* [28], and SitA, from *Salmonella enterica* serovar Typhimurium [29]. A BLASTP analysis revealed that the putative Hi2019 Mn SBP shared 100% identity with the *H. influenzae* 86-028NP protein HfeA, which was initially identified by Harrison and co-workers as a component of an iron-chelate transport system during studies of the OxyR regulon [11]. However, subsequent speculation suggested a possible role in Mn homeostasis, albeit without evidence [30]. The SBP is encoded within the *hfeABCD* operon, which also includes the genes for an ABC-3 family transporter comprised by *hfeB*, which encodes the nucleotide binding domain, and *hfeCD*, which encode the transmembrane domains. Collectively, the bioinformatic analyses suggest that HfeABCD is a putative Mn uptake system and potentially the sole representative of known high-affinity import pathways for this element in Hi2019.

HfeA contributes to Mn homeostasis

The contribution of HfeA to Hi2019 Mn acquisition was investigated by generating an isogenic *hfeA* deletion strain. The Hi2019 Δ*hfeA* strain was complemented using the p601-Hi*hfe*A-comp construct, to generate the Hi2019 Δ*hfeA*::*hfeA* complemented strain. The Hi2019 wild-type and mutant derivative strains were then grown in CDM under different oxygen tensions, aerobic, microaerobic, and anaerobic, to assess the impact of the mutation on bacterial growth kinetics (**Fig. 2**). In aerobic conditions, the Hi2019 Δ*hfeA* strain showed an extended growth delay, approximately 8 h, relative to the wild-type strain (**Fig. 2A**). The final biomass yield of the Δ*hfeA* strain (OD_{600} = 0.87 ± 0.13) was significantly reduced by comparison to the wild-type strain (OD_{600} = 1.56 ± 0.12). The complemented strain showed a modest growth delay of approximately 2 h and its final biomass yield (OD_{600} = 1.33 ± 0.07) was not significantly different from the wild-type parental strain. This can most likely be attributed to differences in expression from the complemented *hfeABCD* operon. During growth in CDM under microaerobic and anaerobic conditions, no differences were observed between the phenotypes of the strains (**Fig. 2B,C**). Although numerous factors are required to support the aerobic growth of Hi2019, these observations show that HfeA also contributes to this process, which can most likely be attributed to a role in Mn uptake.

To investigate this inference, accumulation of the first-row *d*-block elements in the wild-type and derivative Hi2019 strains grown under aerobic conditions in CDM were analyzed (**Fig. 2D-H**). This revealed that ^{55}Mn and ^{59}Co accumulation was significantly reduced by ~3-fold and ~1.6-fold, respectively, in the Δ*hfeA* strain, relative to the wild-type strain (**Fig. 2D,F**). Accumulation of ^{56}Fe, ^{60}Ni, and ^{66}Zn did not significantly differ between the wild-type and Δ*hfeA* strains (**Fig. 2E,G,H**). The complemented strain accumulated *d*-block elements to levels comparable with the wild-type strain, indicating that restoration of *hfeA* recovered ^{55}Mn and ^{59}Co uptake. Collectively, these data show that HfeA contributes to Mn and Co homeostasis under the experimental conditions examined. By contrast, the SBP does not contribute substantially to Fe, Ni, or Zn homeostasis, indicating that other systems are primarily associated with the cellular abundance of these elements in *H. influenzae*

[31-32]. However, it is important to note that in mammalian tissues Co is almost exclusively present in the form of cobalamin, a Co-chelate commonly referred to as Vitamin B_{12}. Bacterial acquisition of host cobalamin occurs via a distinct metal-chelate ABC transporter, BtuCD, and the cluster A-II SBP, BtuF. Accordingly, while HfeA may contribute to *in vitro* Co uptake, it is unlikely to contribute to homeostasis of this element during *in vivo* infection. Thus, these data support a role for HfeA in Mn homeostasis, consistent with the bioinformatic analyses. Further, the absence of other Mn import pathways in the Hi2109 genome suggests that the HfeABCD permease may be primary uptake system for the metal.

Metal-binding properties of *H. influenzae* HfeA

To further investigate Hi2019 HfeA, a recombinant C-terminal dodecahistidine-tagged variant that lacked the predicted signal peptide sequence was generated (residues 23-293). Recombinant HfeA was expressed, purified, and the affinity tag removed by enzymatic cleavage. The protein was resolved by size-exclusion chromatography and analyzed by QTOF LC-MS, which determined a molecular mass of 31.1 kDa that matched the theoretical mass of the protein (**Fig. 3A,B**). Interaction of recombinant, tag-cleaved HfeA with the first-row *d*-block elements (Mn, Fe, Co, Ni, Cu, and Zn) was assessed by incubating the protein with a 10-fold molar excess of each metal, followed by desalting to remove unbound metal ions. Analysis of Mn-treated HfeA showed that the protein bound 1.04 ± 0.30 moles of ^{55}Mn per mol of protein (standard deviation (S.D.); **Fig. 3C**), consistent with a single metal-binding site. However, HfeA was not restricted to interaction with Mn and showed a promiscuous interaction with all *d*-block elements (**Fig. 3C**). The reversibility of metal-binding was then assessed using a 10-fold molar excess of EDTA, a broad-spectrum metal-chelating agent (**Fig. 3C**). This completely reversed binding of ^{55}Mn, ^{56}Fe, and ^{60}Ni (< 20% protein-associated metal), whereas ^{59}Co, ^{63}Cu, and ^{66}Zn showed limited extraction (40-77% protein-associated metal). Taken together, these data suggest that binding of the *d*-block elements Co, Cu, and Zn induced a highly stable, closed conformation of HfeA. To further interrogate interaction of the *d*-block elements with

HfeA, differential scanning fluorimetry (DSF) was performed to determine the melting transition (T_m) temperature of the SBP and how this was influenced by metal binding.

DSF analyses revealed that interaction of any divalent cation (Mn, Fe, Co, Ni, Cu and Zn) with HfeA induced a significant T_m increase (**Table 1**). Therefore, the DSF analyses confirmed that HfeA has a highly promiscuous metal-binding site, consistent with the *in vitro* metal-binding data. However, the degree of thermostabilization conferred by the *d*-block elements varied substantially, with ΔT_m shifts ranging from +11.12 °C [Fe(II)] to +25.12 °C [Zn(II)] (**Table 1**). The ΔT_m data appeared to form two subsets, Fe, Mn, and Ni (ΔT_m < 20 °C) and Co, Cu, Zn (ΔT_m > 20 °C), that were reflective of the reversibility trends observed in the EDTA chelation analyses. Previous single molecule studies of Mn-binding SBPs, such as *Streptococcus pneumoniae* PsaA, have shown that metal ligands that induce highly stabilized protein conformations, i.e. high ΔT_m shifts, decrease the frequency of non-uniform, dynamic transient reopening events [33]. This prevents the SBP ligand-binding site from sampling bulk solvent on physiological timescales, resulting in impaired or abrogated release of the bound metal to the transporter or chelating agents under experimental conditions. Together, the ΔT_m data and limited chelation of HfeA-bound ^{59}Co, ^{63}Cu, and ^{66}Zn by EDTA are consistent with the SBP adopting a metal-bound, closed conformation that is unlikely to release these metal ligands to the transporter. Thus, interaction with these elements could potentially impair the efficiency of Mn uptake due to the formation of non-cognate metal-HfeA complexes. By contrast, the DSF and chelation data for ^{55}Mn, ^{56}Fe, and ^{60}Ni suggest that the HfeBCD transporter could be permissive for uptake of these cations. However, import of these cations via the HfeABCD permease would also depend on the relative abundance of these cations in physiological niches occupied by *H. influenzae*, the contribution of the coordination site within HfeCD to regulating cation import [16], and the presence of other higher affinity importers of these cations, such as energy coupling transporters for Ni [34].

Structural analyses of metal-free *H. influenzae* HfeA

To complement the biophysical characterization of HfeA, the structural properties of SBP were investigated. The crystal structure of recombinant, tag-cleaved mature HfeA in the open, metal-free conformation was determined at 1.77 Å resolution (**Fig. 4A, Table S3**). One HfeA molecule, which also contained part of the cleaved fusion tag (residues 294 – 302), was present in the asymmetric unit. HfeA shows a characteristic cluster A-I SBP fold, comprised by two globular domains (henceforth the N- and C-terminal domains), with each domain consisting of a central four-stranded parallel β-sheet surrounded by four α-helices (**Fig. 4A**). The domains are connected by a rigid α-helical linker (α5, residues 150 – 177), with the interdomain interface forming a site for metal binding. The N-terminal domain also contains a long and disordered β4α4 loop (residues 102 – 127), which includes two short β-strands (β5, β6) and a conserved His residue (His123) involved in metal coordination. Molecular dynamics (MD) simulations indicated that the protein remained stable during the simulations with neither domain of HfeA showing any significant conformational changes over the simulation time course (triplicate 500 ns simulations with the last 250 ns of each trajectory used for analysis). Cluster analysis, using a 2.5 Å cut-off on the backbone atoms of 3,750 structures from the combined trajectories, revealed that HfeA adopted a single dominant conformation. Collectively, these analyses indicate that HfeA has a stable metal-free conformation with no regions of dynamic movement.

Structural analyses of Zn(II)-bound HfeA

Building on the observations above, crystallization of recombinant HfeA was attempted using Mn, its cognate ligand, and Zn, due to its highly favorable thermostabilization properties (**Table 1**) and its frequent occurrence in the crystal structures of orthologous SBPs, such as *S. pneumoniae* PsaA [35]. Despite multiple attempts, Mn(II)-bound HfeA did not yield crystals of sufficient quality for X-ray diffraction. Nevertheless, crystals of Zn(II)-bound HfeA were obtained, and the structure solved at 2.10 Å resolution (**Fig. 4B, Table S3**). Three protein molecules are present in the asymmetric unit of the Zn(II)-bound HfeA crystal structure (Chain A: residues 22 – 293, Chain B: residues 23 – 293,

Chain C: residues 22 – 293). Structural superposition shows that the overall geometry is maintained for all three chains (Cα root mean square deviation [rmsd] values of 0.30 – 0.36 Å between any two chains), with chain C selected for all subsequent analyses. The metal-binding site is located within the interdomain interface, ~13 Å from the molecular surface of the protein. HfeA bound a single Zn(II) ion via tetrahedral coordination by the N-terminal residues His58 (β2α2 loop) and His123 (β4α4 loop), which provide Nε interactions, and the C-terminal residues Glu189 (β7 strand) and Asp264 (β10α9 loop), which provide O-side chain interactions. The distances between the residues and the Zn(II) ion range from 2.1 Å to 2.4 Å (**Fig. 4C**). The stability of Zn(II)-bound HfeA was analyzed by MD and, similar to the metal-free state, the overall fold was stable and did not show any global conformational changes during simulations with the Zn(II) ion remaining within the metal-binding site for the duration of the simulations (average Zn(II)-metal-binding residues distances of: His58-Nε = 2.1 ± 0.01 Å, His123-Nε = 2.2 ± 0.01 Å, Glu189-O = 2.2 ± 0.01 Å, and Asp264-O = 2.2 ± 0.01 Å). Cluster analyses also revealed that across all simulations, a single dominant HfeA conformation was observed. Despite the absence of major global changes in conformation, the MD simulations (**Fig. 4D**) revealed small movements in the orientation of the β2α2 loop, which contains the His58 residue. This resulted in the His58 residue being located >8 Å from the metal-binding site in the metal-free state (**Fig. 4D**). This loop was the only mobile metal-binding region in metal-free HfeA by comparison to the Zn(II)-bound state (**Figure S1**). However, this mobility did not change the solvent accessible surface area of the metal-binding residues (**Table S4**).

Further localized metal-induced structural rearrangements were identified by structural superposition of metal-free HfeA and the Zn(II)-bound state (rmsd value of 2.40 Å, 269 Cα atoms); **Fig. 4E**). This revealed that interaction with the metal resulted in loops β2α2, β7α6, and β10α9 moving inward to the metal-binding site. Concomitant with loop movement, the metal coordinating residues contained therein, His58, Glu189, and Asp264, rotate inwards and towards the Zn(II) ion in the metal-bound structure. Residue His123, which is located on the β4α4 loop, moves slightly away from the metal-

binding site to accommodate metal ion binding. Further comparisons of the two states were performed by superimposing the N-terminal domain of HfeA only. This shows that metal binding induces partial hinge-bending of the α5 helix, which acts as a structural 'backbone' of the SBP, pivoting on residues 164 – 177, resulting in a relative rotation of this region by ~28° about the Z-axis (**Fig. 4E**). Metal-binding also causes a relative rotation of the C-terminal domain by ~24° inwards, resulting in occlusion of the metal-binding site to bulk solvent (**Fig. 4E**).

To better understand the structural relationships between HfeA and related SBPs, HfeA was then compared with twelve bacterial cluster A-I SBPs for which structural data is available (**Figure S2, Table S5**). Structural superposition with the orthologous proteins showed that, in the metal-free state, all SBPs adopted an open conformation with the metal-binding site exposed to bulk solvent (**Figure S3A, Table S5**). In the metal-bound state, all SBPs transitioned to a closed conformation, with the metal ion located within a binding site occluded from bulk solvent (**Figures S3B-C, Table S5**). Despite the differences in the open, metal-free conformations adopted by the distinct SBPs (indicated by the broad range of metal-free Cα rmsd values 1.1 – 3.1 Å; **Table S5**), metal-binding induced transition to a similar overall global conformation (indicated by the lower Cα rmsd values < 2.0 Å). The similar conformations of ligand bound SBPs raise the question of how recognition by their cognate ABC transporter can be achieved, noting that the determinants underlying this process remain poorly defined [16]. Metal coordination by HfeA was then compared to the other SBPs (**Figure S4**). This showed that in the majority of Zn(II)-bound crystal structures, the metal ion was tetrahedrally coordinated by two His residues, one Asp residue, and one Glu residue (O_2N_2), as observed in HfeA. However, there were exceptions that included O_2N_3 pentacoordination in *Treponema pallidum* TroA (**Figure S4C**) and O_1N_3 tetrahedral coordination in *S. pneumoniae* AdcAII [36] and *E. coli* ZnuA (**Figure S4D**). Although we were unable to determine the crystal structure of Mn(II)-bound HfeA, we speculate the cognate ligand would be tetrahedrally coordinated by the same four residues, as exemplified in the closely related *Yersinia pestis* YfeA (**Figure S4E**) and in other Mn-specific SBPs

(**Figures S4F-H)**. Octahedral coordination (O_4N_2) environments for Mn(II)-binding are also frequently reported (**Figures S4I,J**) and are facilitated by the carboxylate residues contributing two (bidentate) metal-coordinating O atoms. In HfeA, the metal-binding site can, theoretically, permit both tetrahedral coordination, as observed for Zn(II), and octahedral geometries due to the number of available ligands. Previously it was shown in the Mn(II)-recruiting SBP from *S. pneumoniae*, PsaA, that abrogating bidentate coordination by the carboxylate residue Asp280, which is comparable to Asp264 in HfeA, profoundly impacted the ability of the SBP to bind Mn(II), while only modestly influencing Zn(II) interaction [17]. Using a similar approach, HfeA Asp264 was mutated to the isosteric, neutral polar amide analogue Asn264. The $HfeA_{D264N}$ variant protein was recombinantly expressed, purified, and characterized for its *in vitro* metal binding properties (**Figure S5**). This revealed that ^{55}Mn binding was abrogated in $HfeA_{D264N}$, consistent with the binding site composition being required to facilitate recruitment of this metal. In contrast, the variant protein remained competent for interaction with ^{66}Zn, albeit to a lesser extent than the wild-type protein. Taken together, these findings provide further support for the role of HfeA in Mn(II) recruitment and indicate that Asp264 directly contributes to coordination of the bound cation. Future studies characterizing the HfeA binding site residues, using the approach shown for $HfeA_{D264N}$, would reveal further insight into their distinct contributions to *d*-block element interaction.

Potential metal-binding mechanism of HfeA

Combining the above observations, we speculate that the metal-binding mechanism of HfeA is distinct from that of other SBPs, such as *E. coli* LivJ [37], *E. coli* ZnuA [38], and *S. pneumoniae* PsaA [17] (**Figure S6**). The interdomain α-helix of cluster A SBPs restricts the extent of conformational motion within this subgroup relative to other SBPs. This contrasts starkly with the Venus' fly-trap ligand-binding mechanism of LivJ, a cluster B SBP from *E. coli* [37], that is facilitated by a shorter interdomain α-helix and flexible loops that permit extensive rotation and movement (~58°, ~17 Å) of the C-terminal domain (**Figure S6A**). In cluster A-I Zn(II)-specific SBPs, such as *E. coli* ZnuA [38], binding

of the metal ion is frequently associated with minor rotation and movement (~5°, ~2 Å) of the C-terminal domain, relative to the ligand-free structure, and a lack of conformational change in the interdomain α-helix (**Figure S6B**). However, in Mn(II)-recruiting SBPs, such as *S. pneumoniae* PsaA, metal binding has been shown to be associated with a partial unwinding of the interdomain α-helix to enable a greater extent of the C-terminal domain rotation and movement (~10°, ~2 Å), relative to the ligand-free structure (**Figure S6C**) [15, 17, 35]. In contrast to PsaA, binding of Zn(II) by HfeA was not associated with breakage of the backbone hydrogen bonds within the interdomain α-helix, but instead a partial bending of the C-terminal portion that enables substantial movement of the C-terminal domain (~24°, ~6 Å), relative to the ligand-free structure. Thus, the metal-binding mechanism of Hi2019 HfeA represents a further variation on the C-terminal domain rotation mechanism used by other cluster A-I SBPs.

HfeA is highly conserved among *H. influenzae* strains

Given the key role of HfeA in Hi2019 Mn accumulation, we next investigated the prevalence and conservation of HfeA and its cognate ABC transporter, HfeBCD, within a global database of 786 publicly available *H. influenzae* genomes that represent human isolates obtained from various sources, including sputum, blood, cerebrospinal fluid, lung, and the middle ear (**Table S6**). Here, the analyses were performed using the Hi2019 amino acid sequences of HfeA (C645_RS02315; WP_005656358.1), HfeB (C645_RS02310; WP_005630123.1), HfeC (C645_RS02305; WP_005666620.1), and HfeD (C645_RS02300; WP_005666622.1) as reference sequences to screen the *H. influenzae* genome database. The HfeA protein was present in 100% of genomes analyzed, with high levels of amino acid sequence conservation (99.0% pairwise identity). Similarly, the HfeBCD proteins were present in 99.8%, 99.8% and 99.9% of *H. influenzae* genomes, respectively, with 96.6% conservation of the *hfeABCD* operon nucleotide sequence (**Table S6**). These data show that HfeA is highly conserved within the *H. influenzae* population and, for the genomes analyzed, 44 unique amino acid variants of HfeA were identified, with Hi2019 *hfeA* encoding the most common

amino acid sequence. Notably, the metal-binding residues were strictly conserved in all HfeA proteins identified, consistent with a critical role in protein function. Variations in the translated HfeA amino acid sequence from the *H. influenzae* genome database were mapped to the Zn(II)-bound HfeA structure, which revealed that residues with high variability were predominantly located within unstructured regions of the protein (**Fig. 5B,C**).

Building on this framework, we further investigated the conservation of HfeA in other species of the genus *Haemophilus*, using a database of 291 publicly available genomes (**Table S6**). Analysis of this database revealed that HfeA orthologs were present in 287 genomes (98.6%) when a screening threshold (70% identity and 70% sequence length) was applied, with a pairwise identity of 84.4%. Phylogenetic analyses of the *hfeA* nucleotide sequence revealed that *H. influenzae* sequences clustered closely with those from *Haemophilus haemolyticus*, *Haemophilus aegyptius*, and *Haemophilus quentini* and exhibited the greatest divergence from *Haemophilus ducreyi*, *Haemophilus parahaemolyticus*, *Haemophilus somnus*, and *Glaesserella parasuis hfeA* sequences (**Fig. 5A**). Carriage of the transporter proteins HfeBC was also high, present in 97.9% and 99.0% of genomes respectively, whereas only 68.4% of non-*influenzae* isolates contained a HfeD ortholog. Although an ortholog of HfeD could not initially be identified in the genomes of *G. parasuis*, *H. somnus*, *H. ducreyi*, and *H. parahaemolyticus*, reducing the screening thresholds (60% sequence identity, 60% sequence length) revealed HfeD orthologs in all but one of these genomes. This indicates that there is greater divergence in the HfeD amino acid sequence among *Haemophilus* species, relative to HfeABC. A nucleotide screen for the *hfeABCD* operon, using representative operon sequences from each species as a reference, revealed its presence in 97.6% of non-*influenzae* genomes, with a pairwise identity of 70.9%. However, in *H. ducreyi*, the *hfeAB* and *hfeCD* genes were positioned at independent locations within the genome. Collectively, these data show that HfeABCD orthologs are encoded in all *Haemophilus* species, and almost all isolates analyzed. This suggests that Mn acquisition is crucial for bacterial survival and/or persistence of *Haemophilus*

populations within host environments and further studies are warranted to investigate the role and essentiality of Mn in this species.

Loss of HfeA compromises oxidative stress management in *H. influenzae*

The phenotypic assays above showed that HfeA and Mn accumulation had a prominent role in supporting aerobic growth of Hi2019. In prokaryotes, Mn is frequently associated with tolerance to oxidative stress, wherein it has been shown to act as a small molecule shield [39], and/or as a cofactor of the metalloenzyme superoxide dismutase (SOD) [30, 40]. Therefore, we investigated the impact of impaired cellular Mn accumulation on the capacity of Hi2019 to tolerate exposure to oxidative stress, using a combination of phenotypic growth studies and microbial killing assays. *H. influenzae* strains only encode a Mn-dependent SOD [41]. Here, we investigated whether Hi2019 Mn-SOD activity was impacted by changes in cellular Mn levels. The bacterial strains were grown in CDM, cell extracts prepared and analyzed using in-gel activity assays. This showed that the Δ*hfeA* strain had reduced Mn-SOD activity, relative to the wild-type and Δ*hfeA*::*hfeA* strains (**Figure S7A**). By contrast, the Mn-independent, cytoplasmic enzyme catalase did not show differences between the strains (**Figure S7B**).

To investigate the physiological consequences of reduced Mn-SOD activity, the Hi2019 wild-type and Δ*hfeA* strains were challenged with two distinct chemical mediators of oxidative stress: *N*,*N*′-dimethyl-4,4′-bipyridinium dichloride (paraquat; 0-25 μM), a viologen that futilely cycles in the cytoplasm, inhibiting NAD(P) reduction and generating superoxide anions; and hydrogen peroxide (0-25 mM), an oxidant and free radical generator (**Fig. 6A-D**). The data showed that, during growth in CDM under microaerobic conditions, paraquat exerted a potent effect on the Δ*hfeA* strain, with growth perturbed at 10 μM and abrogated at 25 μM (**Fig. 6A,B**). By contrast, the wild-type strain only showed a modest reduction in growth and final cell density at 25 μM paraquat. Exposure to hydrogen peroxide mediated a growth delay in the wild-type strain at 10 mM, which was further

exacerbated at 25 mM (**Fig. 6C,D**). The Δ*hfeA* strain showed a similar pattern of impact on growth, although the relative growth delay was shorter for addition of 10 mM hydrogen peroxide.

Consistent with phenotypic growth impact, microbial killing assays with 5 and 10 mM paraquat exerted a significant 1- and 3-$\log_{10}$ reduction, respectively, in survival of the Δ*hfeA* strain, relative to the wild-type and complemented strains (**Fig. 6E**). By contrast, hydrogen peroxide treatment (0 – 750 mM) had a modest impact on survival of the Δ*hfeA* strain compared to the wild-type strain (**Figure S7C**). Complementing this approach, we also examined the impact of paraquat on Hi2019 biofilm formation under microaerobic conditions. Here, the lower paraquat concentration of 1 μM was used, in order to reduce stress to sublethal levels (**Fig. 6F**). In the absence of paraquat stress, all strains produced similar levels of biofilm associated material relative to the density of viable cells (**Fig. 6F**). Upon exposure to 1 μM paraquat, the relative level of biofilm produced by the Δ*hfeA* strain increased significantly by ~4-fold, by comparison to the wild-type and complemented strains (**Fig. 6F, Figure S8**).

Collectively, these data show that Hi2019 has a reduced capacity to tolerate superoxide stress when Mn import is compromised. This can be attributed, at least in part, to the reduced activity of Mn-SOD, which plays a crucial role in the dismutation of oxygen radicals. Although this is predominantly apparent under aerobic conditions, the impact of paraquat on the Δ*hfeA* strain during growth in microaerobic conditions highlights the importance of Mn acquisition for resistance to oxidative stress. Notably, during host-pathogen interaction, oxidative stress can be mediated by the innate immune response and arise from reactive oxygen, nitrogen, and/or chloride species in niches with differing oxygen tensions. The inability to mitigate oxidative stress compromises the viability of Hi2019, although this appears to also enhance biofilm production, which contributes to resisting xenobiotic and chemical stresses, consistent with the observations herein. However, the underlying molecular basis for this phenotypic switch remains to be defined. Irrespective, the importance of Mn to Hi2019

growth and resistance to superoxide stress suggests that it may contribute to bacterial virulence at the host-pathogen interface.

HfeA contributes to survival in phagocytic, but not epithelial cells

To determine the role of HfeA in Hi2019 virulence, the impact of compromised Mn uptake on Hi2019 survival during interaction with human bronchial epithelial cells (16HBE14) and murine bone marrow macrophages (BMMs) was investigated. 16HBE14 cells were infected (MOI 100:1) with the Hi2019 wild-type and derivative strains, incubated for 4 h and 24 h and analyzed for total cell-associated and intracellular bacteria (**Fig. 7A**). This showed that loss of HfeA had no impact on interaction with the 16HBE14 cell line under the experimental conditions investigated. Infection of BMMs (MOI 100:1) with the wild-type and derivative strains for 4 h revealed that the Δ*hfeA* strain had significantly reduced survival of cell-associated and intracellular bacteria, relative to the wild-type strain (**Fig. 7B**). This reduction in survival can likely be attributed to the production of ROS by BMMs as a component of their microbial killing mechanisms [42]. Unexpectedly, although the Hi2019 Δ*hfeA*::*hfeA* strain was not affected for total cell-associated bacteria, intracellular survival appeared to be compromised, by comparison to the wild-type strain. This suggests that, although the complementation restored the overall viability of the strain, it does not completely recapitulate the wild-type phenotype in all conditions.

CONCLUSIONS

This study provides new insights into *H. influenzae* Mn homeostasis and HfeA, the periplasmic SBP associated with the HfeBCD transporter. Biophysical characterization of HfeA showed that it interacted with a broad range of *d*-block elements, similar to other Mn-recruiting cluster A-I SBPs [17]. Despite the apparent promiscuity of the protein in metal-binding, the ready release of Mn cations, in preference to Cu and Zn, support the inference that the primary physiological role of HfeA is in Mn recruitment during *in vivo* infection by *H. influenzae*. Structural studies suggest that HfeA employs a further variation in how cluster A-I SBPs interact with the metal-ligands. The metal-binding site employs a combination of two N atoms, from residues His58 and His123, and at least two O atoms, contributed by residues Glu189 and Asp264. Introduction of the Asn264 point mutation into HfeA disrupted Mn(II) binding, which suggests that Asp264 may provide bidentate coordination for the metal. However, further studies will be required to elucidate the coordination environment of the cognate ligand. Deletion of *hfeA* dysregulated *H. influenzae* Mn homeostasis, which had the concomitant effects of perturbing aerobic growth, reducing adhesion, and invasion of phagocytic cells, and increasing susceptibility to oxidative stress. The impaired survival of the Δ*hfeA* strain upon interaction with phagocytic cells suggests that Mn homeostasis is likely to be crucial for *H. influenzae* resistance to innate immune-mediated oxidative stress. At the host-pathogen interface, exposure to oxidative stress can occur extracellularly, via neutrophil respiratory bursts, or intracellularly, within the phagolysosome of macrophages [43-44]. Nevertheless, our data also highlight that invasion of other cell types, such as bronchial epithelial cells, that do not employ oxidative stress, is not substantially impaired by loss of Mn acquisition. Future studies in relevant models of *H. influenzae* infection would yield further insights into the *in vivo* role of this system. The Mn import pathway of Hi2019 is highly conserved in other *H. influenzae* strains and diverse *Haemophilus* spp. Collectively, these data suggest that HfeA may be a potential target for future therapeutic development approaches to disrupt a crucial pathway that contributes to bacterial resistance against oxidative stress.

METHODS

Bacterial strains, media, and growth experiments

Bacterial strains and plasmids used in this study are listed in **Table S7**. *E. coli* strains were cultured at 37 °C using Luria-Bertani (LB) broth [45] with shaking at 200 rpm or statically on LB agar (1.5% w/v) plates. Where necessary, LB was supplemented with 100 μg mL^{-1} ampicillin, 50 μg mL^{-1} spectinomycin, 100 μg mL^{-1} kanamycin and/or 30 μg mL^{-1} trimethoprim. *H. influenzae* strains were cultured at 37 °C with 5% CO_2 using either liquid or solid Brain Heart Infusion (BHI) (Becton Dickinson) or chemically defined media (CDM; RPMI 1640 [Sigma-Aldrich, R6504-1L] supplemented with: 24 mM sodium bicarbonate, 786 μM uracil, 25 mM HEPES pH 7.5, 10 mM glucose, 7.5 mM inosine, 1 mM sodium pyruvate) [46]. Both BHI and CDM were supplemented with 10 μg mL^{-1} hemin and 10 μg mL^{-1} β-nicotinamide adenine dinucleotide (NAD^+) prior to use [47]. Where appropriate, BHI and CDM were supplemented with 20 μg mL^{-1} kanamycin and/or 50 μg mL^{-1} spectinomycin. Growth experiments using the *H. influenzae* 2019 (Hi2019) strains, wild-type and mutant derivatives, under aerobic, microaerobic and anaerobic conditions in CDM were conducted essentially as previously described using an atmospheric control unit enabled CLARIOstar microplate reader (BMG Labtech) [7]. Atmospheric oxygen (~20% O_2) was used for aerobic conditions; microaerobic conditions used a mixture of 2.8% O_2, 5% CO_2; and anaerobic conditions used 5% CO_2, no oxygen.

Construction and complementation of the Hi2019 Δ*hfeA* strain

To construct the pBlu-Hi2019-hfeA-Km plasmid, upstream and downstream fragments of the Hi2019 *hfeA* (C645_02315) gene were amplified by PCR using primers Hi-hfeA-up F/R and Hi-hfeA-down F/R (**Table S8**). The PCR products were double-digested with EcoRI/BamHI and BamHI/SacI and ligated with EcoRI/SacI digested pBluescript II SK, creating pBlu-Hi2019-hfeA, wherein the *hfeA* coding region contains a BamHI restriction site. To construct pBlu-Hi2019-hfeA-Kan, the kanamycin cassette from plasmid pUC4K was amplified using primers pUC4K-PCR-F/R and

inserted into the BamHI restriction site of pBlue-Hi2019-hfeA (**Table S8**). A plasmid for the complementation of a *hfeA* mutation was constructed using p601.1sp2 [48]. A 4.3 kb PCR-product containing all four genes encoded in the *hfeA* operon and the relevant upstream region was amplified using Flash Phusion Mastermix (Thermo Fisher Scientific) and inserted into the XmaI restriction site of p601.1sp2 generating p601-Hi*hfe*A_comp. All plasmid constructs were verified by a combination of PCR and restriction enzyme digestion. Plasmids were linearized before transformation into Hi2019 [7, 9, 49]. Successful transformations were verified by a combination of PCR and phenotypic analyses.

Bacterial susceptibility testing

Bactericidal assays with Hi2019 and the derivative strains were performed using paraquat (5 mM or 10 mM) or H_2O_2 (up to 0.75 M) and analyzed relative to an untreated control. Briefly, Hi2019 was grown overnight on CDM plates and resuspended to an optical density at 600 nm (OD_{600}) of 1.0 (~ 6×10^8 CFU mL^{-1}) in 1 × phosphate-buffered saline (PBS). Bacterial cells (900 µL) were then combined with 100 µL of 10 × solution (final concentration) of freshly prepared paraquat or H_2O_2. Control conditions used 100 µL of sterile ddH_2O. Reactions were incubated at room temperature for 60 min with orbital shaking at 200 rpm, followed by serial diluted in BHI and plating onto BHI plates for CFU mL^{-1} determination.

Biofilm formation

Biofilm formation and bacterial survival within biofilms were characterized using established protocols [7]. Briefly, Hi2019 from a freshly grown CDM plate was used to inoculate 20 mL CDM (OD_{600} = 0.05) and then incubated at 37 °C with orbital shaking at 200 rpm until early exponential phase was reached (OD_{600} = 0.2-0.3). Cultures were diluted in fresh CDM (OD_{600} = 0.05) and 100 µL $well^{-1}$ added to U-bottom 96-well microtiter plates (TechnoPlas). Plates were incubated statically at 37 °C, 5% CO_2 for 16 h. For anaerobic conditions, plates were incubated in an anaerobic jar at 37 °C with Anaerocult A catalysts (Merck) used to remove oxygen. Biofilm formation was

detected by crystal violet staining [50]. Biofilm viable cell analyses were performed by incubating the biofilm-containing wells with 200 µL of 0.1 mg mL^{-1} proteinase K (Sigma Aldrich) for 10 min at 37 °C. The suspension was then recovered, serially diluted in BHI, and plated onto BHI plates to enable CFU $well^{-1}$ determination.

Superoxide dismutase and catalase activity stains

Colorimetric detection of superoxide dismutase and catalase activity was performed using established methods [51]. Succinctly, *H. influenzae* strains were grown in CDM under microaerobic conditions. Cells were then harvested (10 min, 2,500 relative centrifugal force (rcf), 4 °C) and cellular extracts prepared using BugBuster Mastermix (Merck). Protein concentrations in the extracts were determined by the BCA assay (BCA-1, Sigma-Aldrich), with 2.5 or 40 µg per lane of whole cell extracts loaded on a 10% native PAGE for catalase or superoxide dismutase detection, respectively. Electrophoresis and staining were conducted as described previously [51].

***H. influenzae* infection assays**

Infection of 16HBE14 cells with Hi2019 strains was carried out as described in [7] using a multiplicity of infection (MOI) of 100:1 (*H. influenzae*: 16HBE14). Infections were carried out for either 4 h or 24 h at 37 °C, 5% CO_2. Determination of total and intracellular bacteria was performed using tissue cell lysates generated with 1% (w/v) saponin in combination with (intracellular bacteria) or without (total bacteria) gentamicin treatment (50 mg mL^{-1}, 60 min prior to lysis). Murine bone marrow macrophages (BMMs) were isolated from C57 Black mice using established protocols [52]. Experimental animal procedures were carried out in strict accordance with the recommendations in the QLD Animal Care and Protection Act (2001), and the Australian Code of Practice for the Care and Use of Animals for Scientific Purposes, 8th edition. Protocols were approved by the Animal Care and Ethics Committees of QIMR Berghofer and the University of Queensland under ethics number UQ: 2019/AE000050. In brief, mice were anaesthetized and sacrificed by cervical dislocation, femurs

and tibias were collected and cleaned, and the bone tips removed. The bone cavity was then flushed with BMM medium (RPMI1640 containing 10% heat-inactivated fetal bovine serum, 2 mM L-glutamine [GlutaMAX, Life Technologies], 150 ng mL^{-1} recombinant colony stimulating factor-1 [CSF-1]). BMMs were washed twice with the same medium and divided into eight 100 mm square Petri dishes with 15 mL BMM medium containing 1% (v/v) penicillin/streptomycin (Life Technologies, 10,000 U mL^{-1}). Plates were incubated for six days at 37 °C, 5% CO_2 with the addition of fresh CSF-1 (150 ng mL^{-1}) on day three. On day six, BMMs were removed from the plate, collected by centrifugation (500 × *g*, 5 min), and resuspended in antibiotic-free BMM medium. The BMMs were seeded 1×10^5 cells mL^{-1} per well in 24-well tissue culture plates, infected with the Hi2019 strains using an MOI of 100:1 (bacteria:BMM) and incubated for 4 h [53]. After incubation, BMMs were washed with RPMI1640, treated for 60 min with 10 μg mL^{-1} polymyxin B in BMM medium, and then lysed using 1% (v/v) saponin. Enumeration of bacteria was performed by dilution plating on BHI plates.

Inductively coupled plasma-mass spectrometry (ICP-MS)

Elemental measurements of cellular material and proteins were performed on an Agilent 8900 triple quadrupole inductively coupled plasma-mass spectrometer (ICP-MS, Agilent Technologies). Samples were introduced directly from 1.5 mL polypropylene tubes via an integrated automation system autosampler (Agilent Technologies) using a peristaltic pump. Sample desolvation was performed using a MicroMist nebulizer (Glass Expansion). The instrument was calibrated for elements of interest (**Table S9**) using mixed 0, 5, 10, 25, 50, 100, 250, and 500 μg L^{-1} standard calibration solutions in 1% (v/v) nitric acid (HNO_3) from commercially available certified reference standards (Multi-element Calibration Standard 2A, Agilent Technologies). A reference element solution containing 100 μg L^{-1} yttrium (Y) (Agilent Technologies) was introduced via a T-piece positioned after the peristaltic pump and was used to normalize all measurements. The tuning solution for the instrument contained 1 μg L^{-1} of cerium (Ce), cobalt (Co), lithium (Li), thallium (Tl) and Y in

2% (v/v) HNO_3 (ICP-MS Stock Tuning Solution, Agilent Technologies). Torch position, sample depth adjustment and lens optimization were set according to manufacturer recommendations while all other instrument parameters were optimized during a batch-specific user tune prior to each experimental run (**Table S9**).

Whole cell metal ion accumulation analyses

Elemental content of bacterial strains was determined by ICP-MS essentially as previously described [15, 54]. Briefly, Hi2019 strains were grown to mid-log phase (OD_{600} = 0.3) in CDM and harvested by centrifugation at 2,500 × *g* for 10 min. The cell pellets were subjected to three washes in 5 mM ethylenediaminetetraacetic acid (EDTA) in 1 × PBS, followed by three washes in 1 × PBS to remove adventitious trace metals. The washed cell pellets were then desiccated at 370 K for 18 h. The dry weight of the bacterial cell pellet was determined, and the cellular material digested in 250 µL of 65% (v/v) HNO_3 at 370 K for 20 min. Samples were then centrifuged at 20,000 × *g* for 25 min and the supernatant was diluted in MilliQ-H_2O to a final volume of 1 mL and analyzed in technical triplicate by ICP-MS.

HfeA conservation analysis

The genome of *Haemophilus influenzae* 2019 was screened using TBLASTN [55] for orthologs to previously characterized manganese-recruiting ABC permease solute-binding proteins, natural resistance-associated macrophage proteins (NRAMP), and P-type ATPases from various bacterial species (**Table S1**). Thresholds of ≥ 40% pairwise identity and ≥ 40% query cover were implemented to signify protein sequences of substantial similarity. This search identified a protein, encoded by the annotated gene *hfeA* (C645_02315, WP_005656358.1), as a putative Mn transporter.

A database comprising 786 publicly available *H. influenzae* genomes and 291 Pasteurellaceae genomes was constructed and screened for the presence of HfeA, HfeB, HfeC and HfeD

(WP_005656358.1, WP_005630123.1, WP_005666620.1 and WP_005666622.1) using the TBLASTN screening tool, Screen Assembly (v1.2.7) [56], applying cut-offs of 70% sequence length and 70% sequence identity (**Table S2**). Full-length nucleotide and protein sequences were used for variation analysis by MUSCLE alignment (v3.8.425) [57]. A phylogenetic tree was constructed from aligned nucleotide sequences using the maximum likelihood approach with IQ-Tree (Galaxy v2.1.2) [58]. Trees were visualized using iTOL (v6.5.8) [59]. Aligned amino acid variance was mapped to the Zn(II)-bound Hi2019 HfeA structure (PDB 7U6T) using Chimera (v1.15) [60]. Where stated, the presence of lower similarity proteins was investigated using a screening threshold of 60% sequence length and 60% sequence identity. Prevalence and conservation of *hfeABCD* in the *H. influenzae* and non-*influenzae* genomes was investigated by first identifying the operon in a representative genome from each *Haemophilus* species analyzed. Each representative operon was then used as a reference nucleotide sequence to screen the *H. influenzae* and non-*influenzae* genome databases for the presence of the *hfeABCD* operon sequence using Screen Assembly (v1.2.7), applying cut-offs of 70% sequence length and 70% sequence identity.

Cloning, expression, and purification of HfeA and HfeA$_{D264N}$

The amino acid sequence of Hi2019 HfeA (C645_02315) was analyzed by SignalP 6.0, which predicted that region represented by residues 1-22 encoded a signal peptide [61]. Accordingly, the *hfeA* gene (C645_02315) region encoding residues 23-293, which represents the mature secreted protein, was amplified from Hi2019 genomic DNA by PCR using primers Hfe-IA1F and Hfe-IA1R (**Table S8**) essentially as described previously [16]. Cloning was performed by isothermal assembly [62] into a modified pET30a vector (Novagen, USA) generated by primers ET30-GA1R and ET-GA6F (**Table S8**). This generated the construct pCAM-HfeA-3Chis, which includes the sequence of the mature region of *hfeA* gene product, followed by a C-terminal human rhinovirus (HRV) 3C protease cleavage site and a dodecahistidine tag (**Table S7**). The variant protein, HfeA$_{D264N}$, was generated by site-directed mutagenesis using the QuikChange Lightning Kit (Agilent Technologies) using the pCAM-

HfeA-C3his construct as the template with primers HfeA_D264N_F and HfeA_D264N_R (**Table S8**). Nucleotide sequences of the HfeA and $HfeA_{D264N}$ fusion proteins were confirmed by DNA sequencing. The expression constructs were transformed into *E. coli* XL10 Gold (Agilent Technologies, USA) for propagation or *E. coli* LEMO21 (DE3) (New England Biolabs, Australia) for recombinant protein expression (**Table S7**).

For recombinant protein expression, a single colony was used to inoculate 10 mL of LB medium supplemented with kanamycin (50 μg mL^{-1}). Bacteria were grown overnight at 37 °C, shaking at 200 rpm and diluted into pre-warmed Overnight Express Instant TB medium (Merck) supplemented with 10% (w/v) glycerol and 100 μg mL^{-1} kanamycin. Cultures were then grown at 27 °C for 18 h shaking at 200 rpm in an AirOtop (Thomson Instruments, USA) sealed flask to a final OD_{600} between 30 and 40. Bacterial cells were harvested by centrifugation at 4 °C for 60 min at 40,000 × *g*. The pellet was resuspended and homogenized in 50 mM 3-(N-morpholino) propanesulfonic acid (MOPS) and 200 mM NaCl (pH 7.4) in the presence of one cOmplete EDTA-free protease inhibitor cocktail (Roche, USA) tablet per 50 mL of cells as per manufacturer's recommendations, using a glass dounce homogenizer. Cells were mechanically disrupted using a Constant Systems Cell Disruptor at 30,000 psi at 5 °C, supplemented with DNAse I (Merck, USA). Cellular debris and insoluble membranes were removed by ultracentrifugation at 100,000 × *g* at 4 °C for 1 h. Recombinant HfeA or $HfeA_{D264N}$ proteins were then purified from the clarified lysate by immobilized metal ion affinity chromatography (IMAC). The lysate was applied to a 5 mL HisTrap HP column (Cytiva, USA) on an ÄKTA pure™ FPLC (Cytiva, USA) at 4 °C and washed using 20 column volumes (CVs) of 50 mM MOPS pH 7.4, 200 mM NaCl, 20 mM imidazole. A stepwise gradient was then used to elute non-specific proteins (120 mM imidazole) and recombinant protein (600 mM imidazole). Imidazole was removed from IMAC-purified recombinant HfeA or $HfeA_{D264N}$ by size exclusion chromatography (SEC) on a Superdex 200 10/300 GL column (Cytiva, USA) in 50 mM MOPS pH 7.4, 200 mM NaCl at 4 °C. The dodecahistidine tag was then cleaved by enzymatic digestion using

1 μg hexahistidine-tagged HRV 3C protease to 10 μg recombinant protein. The protein-protease mixture was incubated at 4 °C for 60 min and then purified by IMAC. Here, the digestion mixture was resolved using HisTrap HP column to remove the protease and uncleaved dodecahistidine-tagged protein, with tag-cleaved HfeA eluted in 50 mM MOPS pH 7.4, 200 mM NaCl at 4 °C. Recombinant tag-cleaved HfeA or $HfeA_{D264N}$ was analyzed by 4-12% Bis-Tris PAGE.

Mass spectrometry analysis of intact protein

Confirmation of successful removal of the dodecahistidine tag was performed by intact mass analysis via liquid chromatography-mass spectrometry (LC-MS). Briefly, purified recombinant HfeA was diluted to 50 μg mL^{-1} using aqueous 0.1% formic acid. A 2 μL amount was injected onto a C5 column (50 × 2 mm, 5 μm particle size, 300 Å pore size; Phenomenex) equilibrated with 90% mobile phase A (mobile phase A: 0.1% (v/v) formic acid in MilliQ- H_2O; mobile phase B: 0.1% (v/v) formic acid in 95% (v/v) acetonitrile) held at approximately 60 °C. Separation was performed using a 1200 Infinity HPLC system (Agilent Technologies) running at 95% mobile phase A for 3 min, followed by a linear gradient from 5 % to 95% mobile phase B over 14 min with 95% mobile phase B maintained for 3 min at a flow rate of 0.4 mL min^{-1}. Mass spectrometry acquisition was performed in the positive ion mode on a 6520 Accurate-Mass Q-TOF LC-MS (Agilent Technologies). The following parameters were used on the Q-TOF: nebulizing gas (N_2): 30 psi; drying gas: 10 L min^{-1}; ion source temperature: 325 °C; fragmentor voltage: 150 V; skimmer voltage: 65 V; capillary voltage: 3500 V. The scan range was between 100-3000 *m/z* and resolution of 14,000 *m/z*. Data was acquired and processed using Agilent MassHunter Qualitative Analysis (Agilent Technologies, B.06.00) and deconvoluted using the Maximum Entropy algorithm in MassHunter.

Demetallation of HfeA

Recombinant, tag-cleaved protein (20 mL) was dialyzed against 4 L of sodium acetate pH 4.4 supplemented with 50 mM EDTA at 4 °C for 24 h in a 20 kDa molecular weight cut-off membrane

Slide-A-Lyzer cassette (Thermo Fisher Scientific) The sample was then dialyzed against 4 L of 50 mM MOPS pH 7.2, 200 mM NaCl at 4 °C for a further 24 h. The sample was then recovered, and insoluble material removed by centrifugation at 100,000 × *g* for 20 min at 4 °C. Metal-free, recombinant tag-cleaved protein was then aliquoted, flash-frozen, and stored at 193 K until required. To confirm demetallation, the treated protein sample was analyzed for elemental content. Here, 5 µM protein was digested in 200 µL of 35% (v/v) HNO_3 at 96 °C for 20 min. Samples were then diluted in MilliQ-H_2O to 1 mL in technical triplicates, allowed to cool to room temperature, vortexed then centrifuged at 20,627 × *g* for 25 min to remove insoluble material, and the supernatant collected for ICP-MS analysis. Recombinant tag-cleaved protein was defined as metal-free when the total elemental content represented less than 10% of the protein concentration.

Quantitative metal-binding assays

Metal-free, recombinant tag-cleaved protein (30 µM) was incubated with 10-fold molar excess of *d*-block elements, i.e. Mn(II), Fe(II), Co(II), Ni(II), Cu(II), or Zn(II), in 2 mL of 20 mM MOPS pH 7.2, 100 mM NaCl at 4 °C for 1 h. Following incubation, unbound metal ions were removed using a PD10 column (Cytiva, USA) with recombinant tag-cleaved protein eluted in 20 mM MOPS pH 7.2, 100 mM NaCl. The metal-bound protein was then incubated with 100-fold molar excess of EDTA at 4 °C for 1 h, and desalted again using a PD10 column to separate the protein from the EDTA. Post-treatment, i.e. metal binding and/or metal chelation, the desalted fractions of recombinant protein were digested in 3.5% (v/v) HNO_3 at 96 °C for 15 min. The digested samples were then centrifuged at 20,627 × *g* for 30 min, and the supernatant collected for analysis by ICP-MS to determine the molar ratio of metal to protein using established methods [14, 63].

Differential scanning fluorimetry

Metal-free, recombinant tag-cleaved protein (10 µM) was incubated with a 10-fold molar excess of $MnSO_4$, Fe(II)SO_4, $CoCl_2$, $NiCl_2$, $CuSO_4$, or $ZnSO_4$ at 25 °C in the presence of 5 × SYPRO Orange

(Thermo Fisher Scientific) as described [19]. Samples were then analyzed by differential scanning fluorimetry (DSF) using a QuantStudio Flex 7 Real-Time PCR system (Thermo Fisher Scientific) using a heating rate of 0.1 °C s^{-1} to a final temperature of 97 °C. Fluorescence data were collected at excitation 470 nm/emission 570 nm for buffer only, buffer with metal supplementation, buffer with HfeA, and buffer with HfeA and metal supplementation [17, 21]. After subtraction of background fluorescence of the buffer, the first derivative of the fluorescence data was determined and analyzed using GraphPad Prism (Version 9.4.1) to determine the inflection point of the melting transition. Data from at least three independent experiments were used to determine the $\Delta T_m \pm$ standard deviation (S.D.) of the wild-type HfeA. Statistical significance was determined using one-way ANOVA using a Tukey post-test.

Protein crystallization, crystal structure determination and structural analyses

Initial attempts at crystallizing metal-free and Zn(II)-bound Hi2019 HfeA using sparse-matrix crystallization screens via the hanging-drop vapor-diffusion method were unsuccessful in yielding any protein crystals. Therefore, we hypothesized that the lack of crystals was due to insufficient nucleation. Given that heterogeneous nucleation using a wide variety of heterogeneous nucleating agents has been successful in overcoming the protein nucleation problem [64], we used dried seaweed powder as a heterogeneous nucleant. The heterogeneous nucleation and micro-seeding protocols as previously described [64] were performed for the crystallization of metal-free HfeA. Diffraction quality crystals of metal-free HfeA were obtained in 1.0 M LiCl, 30% (w/v) polyethylene glycol 6000 and 0.1 M citrate (pH 4.0) at 20 °C, with a protein concentration of 10 mg mL^{-1}, using the hanging-drop vapor-diffusion method. To generate the metal-bound state of HfeA, crystals of metal-free HfeA were soaked in the mother liquor supplemented with 100 mM $MnCl_2$ or $ZnCl_2$ for approximately 1 min. Only crystals of Zn(II)-bound HfeA were readily obtained despite screening many $MnCl_2$ concentrations, incubation time, and temperature. Prior to data collection, the harvested crystals were mounted onto Cryoloops (Hampton Research, USA) and briefly soaked in Paratone (Hampton

Research, USA) as the cryoprotectant, before flash-cooling by rapid immersion in liquid nitrogen. The diffraction data were collected on single crystals at the Australian Synchrotron MX2 beamline . To determine crystal structures, the diffraction data were indexed and integrated using *XDS* [65], then scaled and merged in *Aimless* [66]. Initial phases of the metal-free HfeA were obtained by molecular replacement, using a portion (residues 32 – 186) of the metal-free *S. pneumoniae* PsaA crystal structure (PDB ID: 3ZK7) [17] as the search model with *Phenix.Phaser* [67], followed by model building of missing residues in the C-terminal domain with *Coot* [68]. The structures were iteratively refined with *Phenix.Refine* [69] and manually adjusted with *Coot*. Initial phases of the Zn(II)-bound HfeA were obtained by molecular replacement with the Zn(II)-bound *S. pneumoniae* PsaA crystal structure (PDB ID: 1PSZ) [35] as the search model with *Phenix.Phaser*, followed by iterative refinement with *Phenix.Refine* and manual adjustment with *Coot*. Structural analyses (superpositions and metal-ion coordination) were performed in MacPyMOL (v2.5.2 Schrödinger, LLC). Data collection, processing, and structure refinement statistics can be found in **Table S3**.

Molecular dynamics simulations

The starting structures for the Zn(II)-bound and metal-free protein were extracted from their respective crystal structures. All water molecules and ions present in the crystal structures were removed. His residues were modelled in their protonated state. The protein structure was placed in a 9.5 × 7.5 × 7.0 nm rectangular box and solvated with water molecules. Na^+ and Cl^- ions were used to neutralize the protein charge and obtain a salt concentration of 100 mM NaCl. The system was energy-minimized using the steepest descent algorithm, followed by a 5 ns NVT and a 5 ns NPT simulation. For the NPT production runs, the metal-free protein was simulated for 500 ns, while the Zn(II)-bound protein was simulated for 1,500 ns. The lengths of the simulation were determined based on monitoring convergence of root-means square (rms) vs time for all heavy atoms in the protein. For both systems, three independent runs were carried out, starting from different initial velocities that were assigned from Maxwellian distributions at 298 K. Equilibration was monitored

with RMSD vs time plots where RMSD was calculated using all heavy atoms in the system. All simulations were carried out using the GROMACS package version 5.0.1 [70-71]. Periodic boundary conditions were applied in all three directions. The time step was 2 fs, and the neighbor list was updated every 10 steps. The system temperature was kept at 298 K using a V-rescale thermostat with a coupling time constant of 0.1 ps and separate coupling of the protein and solvent (water and ions). The system pressure was maintained at 1 bar using a Parrinello-Rahman barostat [72] with isotropic pressure coupling and coupling time constant of 2.0 ps. For short-range interactions, a cut-off of 1.0 nm was used for both the van der Waals and electrostatic interactions in Verlet scheme [73]. Long-range electrostatics were described with a Particle-mesh Ewald algorithm [74] using a grid spacing 0.16 and a cubic interpolation of 4. The bond lengths were constrained with the LINCS constraints algorithm [75]. All analyses were performed using GROMACS tools and custom python scripts written with MDAnalysis library [76]. Unless otherwise stated, properties were calculated using the last 250 ns from the trajectory of each independent simulation. Cluster analysis was carried out using the algorithm as implemented in the GROMACS tools gmx cluster [77], with a backbone RMSD cut-off of 2.5 Å. The systems were visualized using VMD [78].

Statistical analysis

Data represent the mean of biological triplicates [± standard error of the mean (SEM)] unless otherwise stated. Statistical analyses were performed using a two-tailed, unpaired Student's t-test when comparing two datasets, or a one-way or two-way ANOVA, as appropriate, for comparisons of multiple datasets. Multiple comparisons used post hoc tests as noted, with symbols for Student's t-test and ANOVA tests (ns, non-significant; *, $P < 0.05$; **, $P < 0.01$; ***, $P < 0.001$; and ****, $P < 0.0001$).

ANCILLARY INFORMATION

Supporting Information Available: Elemental analysis of growth media; Analysis of the Hi2019 genome for transporters with homology to manganese uptake systems; X-ray crystallography data collection, processing, and refinement statistics; Solvent accessible surface area of HfeA metal-binding residues; Structurally characterized Hi2019 HfeA orthologs; Genomic screening of *Haemophilus* spp.; Strains and plasmids used in this study; Oligonucleotide sequences used in this study; ICP-MS operating parameters; Root mean square fluctuation analyses of metal-free and Zn(II)-bound HfeA; Multiple sequence alignment of Hi2019 HfeA with 12 bacterial cluster A-I SBP orthologs; Structural comparisons of HfeA with metal-free and metal-bound cluster A-I SBPs; Structural comparison of cluster A-I SBP metal-binding sites; *In vitro* metal-binding properties of $HfeA_{D264N}$; Comparison of SBP ligand-binding mechanisms; Effect of HfeA loss in enzymatic-mediated oxidative stress management; Role of HfeA in oxidative stress resistance and biofilm formation.

PDB ID Codes:

The accession codes for the structures deposited in the Protein Data Bank are 7U6S (metal-free HfeA) and 7U6T (zinc-bound HfeA). Authors will release the atomic coordinates and experimental data upon article publication.

Corresponding Author Information:

Ulrike Kappler, School of Chemistry and Molecular Biosciences, The University of Queensland, Brisbane, Queensland 4072, Australia. E-mail: u.kappler1@uq.edu.au; Christopher A. McDevitt, Department of Microbiology and Immunology, The Peter Doherty Institute for Infection and Immunity, The University of Melbourne, Melbourne, Victoria, 3000, Australia. E-mail: christopher.mcdevitt@unimelb.edu.au

Acknowledgements:

We thank Dr Ama-Tawiah Essilfie for assistance with the murine experiments and Professor Alastair McEwan (University of Queensland, Australia) and Professor Megan Maher (University of Melbourne, Australia) for discussions and feedback on the manuscript. We acknowledge use and thank the staff of the Australian Synchrotron MX beamlines, the UQ-ROCX (University of Queensland Remote Operation Crystallization and X-Ray Diffraction) Facility at the Centre for Microscopy and Microanalysis, and the Melbourne Mass Spectrometry and Proteomics Facility (MMSPF) at the Bio21 Molecular Science and Biotechnology Institute, the University of Melbourne. This research was undertaken with the assistance of resources and services from the National Computational Infrastructure (NCI), which is supported by the Australian Government and by resources provided by The Pawsey Supercomputing Centre with funding from the Australian Government and the Government of Western Australia. This research was also undertaken using the LIEF HPC-GPGPU Facility hosted at the University of Melbourne. This Facility was established with the assistance of Australian Research Council (ARC) LIEF Grant LE170100200. This work was supported by the National Health and Medical Research Council (NHMRC) grants 1071659 to B.K., 1122582 to C.A.M., 1180826 to B.K. and C.A.M and 1158451 to U.K., A.G.M. and A-T.E. E.D. is a UTS Chancellor's Postdoctoral Fellow, B.K. is an ARC Laureate Fellow (FL180100109), and C.A.M. is an ARC Future Fellow (FT170100006). The content of this study is solely the responsibility of the authors and does not necessarily represent the official views of the funding bodies.

Author Contributions:

KG, BK, ED, UK, and CAM designed the study. KG, SLN and JW performed the biochemical and biophysical studies of HfeA and $HfeA_{D264N}$. KG and AG performed the ICP-MS analyses. JJW, JW and CAM generated the expression constructs. MN, DE, and ZJY performed the molecular microbiology and infection assays. EAM performed the bioinformatic studies. ZL, DHYN, DE, and

JG performed the structural studies. ED and SIH performed the molecular dynamics studies. KG, UK, and CAM wrote the first draft of the manuscript with specific sections contributed by EAM, DHYN and ED. KG, BK, UK, and CAM reviewed and revised the manuscript text. All authors read and approved the submitted version.

Abbreviations Used:

Hi2019, *Haemophilus influenzae* strain 2019

REFERENCES

(1) Van Eldere, J.; Slack, M. P.; Ladhani, S.; Cripps, A. W., Non-typeable *Haemophilus influenzae*, an under-recognised pathogen. *Lancet Infect Dis* **2014,** *14* (12), 1281-92. DOI: 10.1016/S1473-3099(14)70734-0.

(2) Ahn, D.; Prince, A., Participation of the IL-10RB Related Cytokines, IL-22 and IFN-lambda in Defense of the Airway Mucosal Barrier. *Front Cell Infect Microbiol* **2020,** *10*, 300. DOI: 10.3389/fcimb.2020.00300.

(3) Lansbury, L.; Lim, B.; Baskaran, V.; Lim, W. S., Co-infections in people with COVID-19: a systematic review and meta-analysis. *J Infect* **2020,** *81* (2), 266-275. DOI: 10.1016/j.jinf.2020.05.046.

(4) Langereis, J. D.; Cremers, A. J. H.; Vissers, M.; van Beek, J.; Meis, J. F.; de Jonge, M. I., Nontypeable *Haemophilus influenzae* Invasive Blood Isolates Are Mainly Phosphorylcholine Negative and Show Decreased Complement-Mediated Killing That Is Associated with Lower Binding of IgM and CRP in Comparison to Colonizing Isolates from the Oropharynx. *Infect Immun* **2019,** *87* (2), e00604-18. DOI: 10.1128/IAI.00604-18.

(5) World Health Organization Global priority list of antibiotic-resistant bacteria to guide research, discovery, and development of new antibiotics. http://www.who.int/medicines/publications/global-priority-list-antibiotic-resistant-bacteria/en/ (accessed 01/02/22).

(6) Dhouib, R.; Nasreen, M.; Othman, D.; Ellis, D.; Lee, S.; Essilfie, A. T.; Hansbro, P. M.; McEwan, A. G.; Kappler, U., The DmsABC Sulfoxide Reductase Supports Virulence in Non-typeable *Haemophilus influenzae*. *Front Microbiol* **2021,** *12*, 686833. DOI: 10.3389/fmicb.2021.686833.

(7) Dhouib, R.; Othman, D. S.; Lin, V.; Lai, X. J.; Wijesinghe, H. G.; Essilfie, A. T.; Davis, A.; Nasreen, M.; Bernhardt, P. V.; Hansbro, P. M.; McEwan, A. G.; Kappler, U., A Novel, Molybdenum-Containing Methionine Sulfoxide Reductase Supports Survival of *Haemophilus*

influenzae in an *In vivo* Model of Infection. *Front Microbiol* **2016,** *7*, 1743. DOI: 10.3389/fmicb.2016.01743.

(8) Harrison, A.; Baker, B. D.; Munson, R. S., Jr., Overlapping and complementary oxidative stress defense mechanisms in nontypeable *Haemophilus influenzae*. *J Bacteriol* **2015,** *197* (2), 277-85. DOI: 10.1128/JB.01973-14.

(9) Nasreen, M.; Dhouib, R.; Hosmer, J.; Wijesinghe, H. G. S.; Fletcher, A.; Mahawar, M.; Essilfie, A. T.; Blackall, P. J.; McEwan, A. G.; Kappler, U., Peptide Methionine Sulfoxide Reductase from *Haemophilus influenzae* Is Required for Protection against HOCl and Affects the Host Response to Infection. *ACS Infect Dis* **2020,** *6* (7), 1928-1939. DOI: 10.1021/acsinfecdis.0c00242.

(10) Juneau, R. A.; Pang, B.; Armbruster, C. E.; Murrah, K. A.; Perez, A. C.; Swords, W. E., Peroxiredoxin-glutaredoxin and catalase promote resistance of nontypeable *Haemophilus influenzae* 86-028NP to oxidants and survival within neutrophil extracellular traps. *Infect Immun* **2015,** *83* (1), 239-46. DOI: 10.1128/IAI.02390-14.

(11) Harrison, A.; Ray, W. C.; Baker, B. D.; Armbruster, D. W.; Bakaletz, L. O.; Munson, R. S., Jr., The OxyR regulon in nontypeable *Haemophilus influenzae*. *J Bacteriol* **2007,** *189* (3), 1004-12. DOI: 10.1128/JB.01040-06.

(12) Harrison, A.; Santana, E. A.; Szelestey, B. R.; Newsom, D. E.; White, P.; Mason, K. M., Ferric uptake regulator and its role in the pathogenesis of nontypeable *Haemophilus influenzae*. *Infect Immun* **2013,** *81* (4), 1221-33. DOI: 10.1128/IAI.01227-12.

(13) Nasreen, M.; Fletcher, A.; Hosmer, J.; Zhong, Q.; Essilfie, A. T.; McEwan, A. G.; Kappler, U., The Alternative Sigma Factor RpoE2 Is Involved in the Stress Response to Hypochlorite and *in vivo* Survival of *Haemophilus influenzae*. *Front Microbiol* **2021,** *12*, 637213. DOI: 10.3389/fmicb.2021.637213.

(14) Brazel, E. B.; Tan, A.; Neville, S. L.; Iverson, A. R.; Udagedara, S. R.; Cunningham, B. A.; Sikanyika, M.; De Oliveira, D. M. P.; Keller, B.; Bohlmann, L.; El-Deeb, I. M.; Ganio, K.; Eijkelkamp, B. A.; McEwan, A. G.; von Itzstein, M.; Maher, M. J.; Walker, M. J.; Rosch, J. W.;

McDevitt, C. A., Dysregulation of *Streptococcus pneumoniae* zinc homeostasis breaks ampicillin resistance in a pneumonia infection model. *Cell Rep* **2022,** *38* (2), 110202. DOI: 10.1016/j.celrep.2021.110202.

(15) McDevitt, C. A.; Ogunniyi, A. D.; Valkov, E.; Lawrence, M. C.; Kobe, B.; McEwan, A. G.; Paton, J. C., A molecular mechanism for bacterial susceptibility to zinc. *PLoS Pathog* **2011,** *7* (11), e1002357. DOI: 10.1371/journal.ppat.1002357.

(16) Neville, S. L.; Sjohamn, J.; Watts, J. A.; MacDermott-Opeskin, H.; Fairweather, S. J.; Ganio, K.; Carey Hulyer, A.; McGrath, A. P.; Hayes, A. J.; Malcolm, T. R.; Davies, M. R.; Nomura, N.; Iwata, S.; O'Mara, M. L.; Maher, M. J.; McDevitt, C. A., The structural basis of bacterial manganese import. *Sci Adv* **2021,** *7* (32), eabg3980. DOI: 10.1126/sciadv.abg3980.

(17) Couñago, R. M.; Ween, M. P.; Begg, S. L.; Bajaj, M.; Zuegg, J.; O'Mara, M. L.; Cooper, M. A.; McEwan, A. G.; Paton, J. C.; Kobe, B.; McDevitt, C. A., Imperfect coordination chemistry facilitates metal ion release in the Psa permease. *Nat Chem Biol* **2014,** *10* (1), 35-41. DOI: 10.1038/nchembio.1382.

(18) Alquethamy, S.; Ganio, K.; Luo, Z.; Hossain, S. I.; Hayes, A. J.; Ve, T.; Davies, M. R.; Deplazes, E.; Kobe, B.; McDevitt, C. A., Structural and biochemical characterization of *Acinetobacter baumannii* ZnuA. *J Inorg Biochem* **2022,** *231*, 111787. DOI: 10.1016/j.jinorgbio.2022.111787.

(19) Župan, M. L.; Luo, Z.; Ganio, K.; Pederick, V. G.; Neville, S. L.; Deplazes, E.; Kobe, B.; McDevitt, C. A., Conformation of the Solute-Binding Protein AdcAII Influences Zinc Uptake in *Streptococcus pneumoniae*. *Front Cell Infect Microbiol* **2021,** *11*, 729981. DOI: 10.3389/fcimb.2021.729981.

(20) Luo, Z.; Morey, J. R.; Deplazes, E.; Motygullina, A.; Tan, A.; Ganio, K.; Neville, S. L.; Eleftheriadis, N.; Isselstein, M.; Pederick, V. G.; Paton, J. C.; Cordes, T.; Harmer, J. R.; Kobe, B.; McDevitt, C. A., A Trap-Door Mechanism for Zinc Acquisition by *Streptococcus pneumoniae* AdcA. *mBio* **2021,** *12* (1), e01958-20. DOI: 10.1128/mBio.01958-20.

(21) Begg, S. L.; Eijkelkamp, B. A.; Luo, Z.; Counago, R. M.; Morey, J. R.; Maher, M. J.; Ong, C. L.; McEwan, A. G.; Kobe, B.; O'Mara, M. L.; Paton, J. C.; McDevitt, C. A., Dysregulation of transition metal ion homeostasis is the molecular basis for cadmium toxicity in *Streptococcus pneumoniae*. *Nat Commun* **2015,** *6*, 6418. DOI: 10.1038/ncomms7418.

(22) Handke, L. D.; Gribenko, A. V.; Timofeyeva, Y.; Scully, I. L.; Anderson, A. S., MntC-Dependent Manganese Transport Is Essential for *Staphylococcus aureus* Oxidative Stress Resistance and Virulence. *mSphere* **2018,** *3* (4), e00336-18. DOI: 10.1128/mSphere.00336-18.

(23) Ouyang, Z.; He, M.; Oman, T.; Yang, X. F.; Norgard, M. V., A manganese transporter, BB0219 (BmtA), is required for virulence by the Lyme disease spirochete, *Borrelia burgdorferi*. *Proc Natl Acad Sci U S A* **2009,** *106* (9), 3449-54. DOI: 10.1073/pnas.0812999106.

(24) Andreini, C.; Bertini, I.; Cavallaro, G.; Holliday, G. L.; Thornton, J. M., Metal ions in biological catalysis: from enzyme databases to general principles. *J Biol Inorg Chem* **2008,** *13* (8), 1205-18. DOI: 10.1007/s00775-008-0404-5.

(25) Martin, J. E.; Waters, L. S.; Storz, G.; Imlay, J. A., The *Escherichia coli* small protein MntS and exporter MntP optimize the intracellular concentration of manganese. *PLoS Genet* **2015,** *11* (3), e1004977. DOI: 10.1371/journal.pgen.1004977.

(26) Ouyang, A.; Gasner, K. M.; Neville, S. L.; McDevitt, C. A.; Frawley, E. R., MntP and YiiP Contribute to Manganese Efflux in *Salmonella enterica* Serovar Typhimurium under Conditions of Manganese Overload and Nitrosative Stress. *Microbiol Spectr* **2022,** *10* (1), e0131621. DOI: 10.1128/spectrum.01316-21.

(27) Papp-Wallace, K. M.; Maguire, M. E., Manganese transport and the role of manganese in virulence. *Annu Rev Microbiol* **2006,** *60*, 187-209. DOI: 10.1146/annurev.micro.60.080805.142149.

(28) Bearden, S. W.; Perry, R. D., The Yfe system of *Yersinia pestis* transports iron and manganese and is required for full virulence of plague. *Mol Microbiol* **1999,** *32* (2), 403-14. DOI: 10.1046/j.1365-2958.1999.01360.x.

(29) Kehres, D. G.; Janakiraman, A.; Slauch, J. M.; Maguire, M. E., SitABCD is the alkaline Mn(2+) transporter of *Salmonella enterica* serovar Typhimurium. *J Bacteriol* **2002,** *184* (12), 3159-66. DOI: 10.1128/JB.184.12.3159-3166.2002.

(30) Harrison, A.; Bakaletz, L. O.; Munson, R. S., Jr., *Haemophilus influenzae* and oxidative stress. *Front Cell Infect Microbiol* **2012,** *2*, 40. DOI: 10.3389/fcimb.2012.00040.

(31) Whitby, P. W.; Seale, T. W.; VanWagoner, T. M.; Morton, D. J.; Stull, T. L., The iron/heme regulated genes of *Haemophilus influenzae*: comparative transcriptional profiling as a tool to define the species core modulon. *BMC Genomics* **2009,** *10*, 6. DOI: 10.1186/1471-2164-10-6.

(32) Duell, B. L.; Su, Y. C.; Riesbeck, K., Host-pathogen interactions of nontypeable *Haemophilus influenzae*: from commensal to pathogen. *FEBS Lett* **2016,** *590* (21), 3840-3853. DOI: 10.1002/1873-3468.12351.

(33) de Boer, M.; Gouridis, G.; Vietrov, R.; Begg, S. L.; Schuurman-Wolters, G. K.; Husada, F.; Eleftheriadis, N.; Poolman, B.; McDevitt, C. A.; Cordes, T., Conformational and dynamic plasticity in substrate-binding proteins underlies selective transport in ABC importers. *eLife* **2019,** *8*, e44652. DOI: 10.7554/eLife.44652.

(34) Kirsch, F.; Eitinger, T., Transport of nickel and cobalt ions into bacterial cells by S components of ECF transporters. *Biometals* **2014,** *27* (4), 653-60. DOI: 10.1007/s10534-014-9738-3.

(35) Lawrence, M. C.; Pilling, P. A.; Epa, V. C.; Berry, A. M.; Ogunniyi, A. D.; Paton, J. C., The crystal structure of pneumococcal surface antigen PsaA reveals a metal-binding site and a novel structure for a putative ABC-type binding protein. *Structure* **1998,** *6* (12), 1553-61. DOI: 10.1016/s0969-2126(98)00153-1.

(36) Loisel, E.; Jacquamet, L.; Serre, L.; Bauvois, C.; Ferrer, J. L.; Vernet, T.; Di Guilmi, A. M.; Durmort, C., AdcAII, a new pneumococcal Zn-binding protein homologous with ABC transporters: biochemical and structural analysis. *J Mol Biol* **2008,** *381* (3), 594-606. DOI: 10.1016/j.jmb.2008.05.068.

(37) Mao, B.; Pear, M. R.; McCammon, J. A.; Quiocho, F. A., Hinge-bending in L-arabinose-binding protein. The "Venus's-flytrap" model. *J Biol Chem* **1982,** *257* (3), 1131-3.

(38) Chandra, B. R.; Yogavel, M.; Sharma, A., Structural analysis of ABC-family periplasmic zinc binding protein provides new insights into mechanism of ligand uptake and release. *J Mol Biol* **2007,** *367* (4), 970-82. DOI: 10.1016/j.jmb.2007.01.041.

(39) Daly, M. J.; Gaidamakova, E. K.; Matrosova, V. Y.; Kiang, J. G.; Fukumoto, R.; Lee, D. Y.; Wehr, N. B.; Viteri, G. A.; Berlett, B. S.; Levine, R. L., Small-molecule antioxidant proteome-shields in *Deinococcus radiodurans*. *PLoS One* **2010,** *5* (9), e12570. DOI: 10.1371/journal.pone.0012570.

(40) D'Mello, R. A.; Langford, P. R.; Kroll, J. S., Role of bacterial Mn-cofactored superoxide dismutase in oxidative stress responses, nasopharyngeal colonization, and sustained bacteremia caused by *Haemophilus influenzae* type b. *Infect Immun* **1997,** *65* (7), 2700-6. DOI: 10.1128/iai.65.7.2700-2706.1997.

(41) Kroll, J. S.; Langford, P. R.; Saah, J. R.; Loynds, B. M., Molecular and genetic characterization of superoxide dismutase in *Haemophilus influenzae* type b. *Mol Microbiol* **1993,** *10* (4), 839-48. DOI: 10.1111/j.1365-2958.1993.tb00954.x.

(42) Flannagan, R. S.; Cosio, G.; Grinstein, S., Antimicrobial mechanisms of phagocytes and bacterial evasion strategies. *Nat Rev Microbiol* **2009,** *7* (5), 355-66. DOI: 10.1038/nrmicro2128.

(43) Kehl-Fie, T. E.; Chitayat, S.; Hood, M. I.; Damo, S.; Restrepo, N.; Garcia, C.; Munro, K. A.; Chazin, W. J.; Skaar, E. P., Nutrient metal sequestration by calprotectin inhibits bacterial superoxide defense, enhancing neutrophil killing of *Staphylococcus aureus*. *Cell Host Microbe* **2011,** *10* (2), 158-64. DOI: 10.1016/j.chom.2011.07.004.

(44) Eijkelkamp, B. A.; Morey, J. R.; Neville, S. L.; Tan, A.; Pederick, V. G.; Cole, N.; Singh, P. P.; Ong, C. Y.; Gonzalez de Vega, R.; Clases, D.; Cunningham, B. A.; Hughes, C. E.; Comerford, I.; Brazel, E. B.; Whittall, J. J.; Plumptre, C. D.; McColl, S. R.; Paton, J. C.; McEwan, A. G.;

Doble, P. A.; McDevitt, C. A., Dietary zinc and the control of *Streptococcus pneumoniae* infection. *PLoS Pathog* **2019,** *15* (8), e1007957. DOI: 10.1371/journal.ppat.1007957.

(45) Ausubel, F. M., *Short protocols in molecular biology: a compendium of methods from current protocols in molecular biology*. 5 ed.; Wiley: 2002.

(46) Coleman, H. N.; Daines, D. A.; Jarisch, J.; Smith, A. L., Chemically defined media for growth of *Haemophilus influenzae* strains. *J Clin Microbiol* **2003,** *41* (9), 4408-10. DOI: 10.1128/JCM.41.9.4408-4410.2003.

(47) Johnston, J. W., Laboratory growth and maintenance of *Haemophilus influenzae*. *Curr Protoc Microbiol* **2010,** *Chapter 6*, Unit 6D 1. DOI: 10.1002/9780471729259.mc06d01s18.

(48) Johnston, J. W.; Zaleski, A.; Allen, S.; Mootz, J. M.; Armbruster, D.; Gibson, B. W.; Apicella, M. A.; Munson, R. S., Jr., Regulation of sialic acid transport and catabolism in *Haemophilus influenzae*. *Mol Microbiol* **2007,** *66* (1), 26-39. DOI: 10.1111/j.1365-2958.2007.05890.x.

(49) Poje, G.; Redfield, R. J., Transformation of *Haemophilus influenzae*. In *Haemophilus influenzae Protocols*, Herbert, M. A.; Hood, D. W.; Moxon, E. R., Eds. Humana Press: Totowa, NJ, 2003; pp 57-70. DOI: 10.1385/1-59259-321-6:57.

(50) Schembri, M. A.; Klemm, P., Biofilm formation in a hydrodynamic environment by novel *fimH* variants and ramifications for virulence. *Infect Immun* **2001,** *69* (3), 1322-8. DOI: 10.1128/IAI.69.3.1322-1328.2001.

(51) Weydert, C. J.; Cullen, J. J., Measurement of superoxide dismutase, catalase and glutathione peroxidase in cultured cells and tissue. *Nat Protoc* **2010,** *5* (1), 51-66. DOI: 10.1038/nprot.2009.197.

(52) Tushinski, R. J.; Oliver, I. T.; Guilbert, L. J.; Tynan, P. W.; Warner, J. R.; Stanley, E. R., Survival of mononuclear phagocytes depends on a lineage-specific growth factor that the differentiated cells selectively destroy. *Cell* **1982,** *28* (1), 71-81. DOI: 10.1016/0092-8674(82)90376-2.

(53) Ackland, J.; Heinson, A. I.; Cleary, D. W.; Christodoulides, M.; Wilkinson, T. M. A.; Staples, K. J., Dual RNASeq Reveals NTHi-Macrophage Transcriptomic Changes During Intracellular Persistence. *Front Cell Infect Microbiol* **2021,** *11*, 723481. DOI: 10.3389/fcimb.2021.723481.

(54) Eijkelkamp, B. A.; Morey, J. R.; Ween, M. P.; Ong, C. L.; McEwan, A. G.; Paton, J. C.; McDevitt, C. A., Extracellular zinc competitively inhibits manganese uptake and compromises oxidative stress management in *Streptococcus pneumoniae*. *PLoS One* **2014,** *9* (2), e89427. DOI: 10.1371/journal.pone.0089427.

(55) Gertz, E. M.; Yu, Y. K.; Agarwala, R.; Schaffer, A. A.; Altschul, S. F., Composition-based statistics and translated nucleotide searches: improving the TBLASTN module of BLAST. *BMC Biol* **2006,** *4*, 41. DOI: 10.1186/1741-7007-4-41.

(56) Davies, M. R.; McIntyre, L.; Mutreja, A.; Lacey, J. A.; Lees, J. A.; Towers, R. J.; Duchene, S.; Smeesters, P. R.; Frost, H. R.; Price, D. J.; Holden, M. T. G.; David, S.; Giffard, P. M.; Worthing, K. A.; Seale, A. C.; Berkley, J. A.; Harris, S. R.; Rivera-Hernandez, T.; Berking, O.; Cork, A. J.; Torres, R.; Lithgow, T.; Strugnell, R. A.; Bergmann, R.; Nitsche-Schmitz, P.; Chhatwal, G. S.; Bentley, S. D.; Fraser, J. D.; Moreland, N. J.; Carapetis, J. R.; Steer, A. C.; Parkhill, J.; Saul, A.; Williamson, D. A.; Currie, B. J.; Tong, S. Y. C.; Dougan, G.; Walker, M. J., Atlas of group A streptococcal vaccine candidates compiled using large-scale comparative genomics. *Nat Genet* **2019,** *51* (6), 1035-1043. DOI: 10.1038/s41588-019-0417-8.

(57) Edgar, R. C., MUSCLE: multiple sequence alignment with high accuracy and high throughput. *Nucleic Acids Res* **2004,** *32* (5), 1792-7. DOI: 10.1093/nar/gkh340.

(58) Minh, B. Q.; Schmidt, H. A.; Chernomor, O.; Schrempf, D.; Woodhams, M. D.; von Haeseler, A.; Lanfear, R., IQ-TREE 2: New Models and Efficient Methods for Phylogenetic Inference in the Genomic Era. *Mol Biol Evol* **2020,** *37* (5), 1530-1534. DOI: 10.1093/molbev/msaa015.

(59) Letunic, I.; Bork, P., Interactive Tree Of Life (iTOL) v5: an online tool for phylogenetic tree display and annotation. *Nucleic Acids Res* **2021,** *49* (W1), W293-W296. DOI: 10.1093/nar/gkab301.

(60) Pettersen, E. F.; Goddard, T. D.; Huang, C. C.; Couch, G. S.; Greenblatt, D. M.; Meng, E. C.; Ferrin, T. E., UCSF Chimera--a visualization system for exploratory research and analysis. *J Comput Chem* **2004,** *25* (13), 1605-12. DOI: 10.1002/jcc.20084.

(61) Teufel, F.; Almagro Armenteros, J. J.; Johansen, A. R.; Gislason, M. H.; Pihl, S. I.; Tsirigos, K. D.; Winther, O.; Brunak, S.; von Heijne, G.; Nielsen, H., SignalP 6.0 predicts all five types of signal peptides using protein language models. *Nat Biotechnol* **2022,** *40* (7), 1023-1025. DOI: 10.1038/s41587-021-01156-3.

(62) Gibson, D. G.; Young, L.; Chuang, R. Y.; Venter, J. C.; Hutchison, C. A., 3rd; Smith, H. O., Enzymatic assembly of DNA molecules up to several hundred kilobases. *Nat Methods* **2009,** *6* (5), 343-5. DOI: 10.1038/nmeth.1318.

(63) Neville, S. L.; Eijkelkamp, B. A.; Lothian, A.; Paton, J. C.; Roberts, B. R.; Rosch, J. W.; McDevitt, C. A., Cadmium stress dictates central carbon flux and alters membrane composition in *Streptococcus pneumoniae*. *Commun Biol* **2020,** *3* (1), 694. DOI: 10.1038/s42003-020-01417-y.

(64) Luo, Z.; Morey, J. R.; McDevitt, C. A.; Kobe, B., Heterogeneous nucleation is required for crystallization of the ZnuA domain of pneumococcal AdcA. *Acta Crystallogr F Struct Biol Commun* **2015,** *71* (Pt 12), 1459-64. DOI: 10.1107/S2053230X15021330.

(65) Kabsch, W., Xds. *Acta Crystallogr D Biol Crystallogr* **2010,** *66* (Pt 2), 125-32. DOI: 10.1107/S0907444909047337.

(66) Evans, P. R.; Murshudov, G. N., How good are my data and what is the resolution? *Acta Crystallogr D Biol Crystallogr* **2013,** *69* (Pt 7), 1204-14. DOI: 10.1107/S0907444913000061.

(67) McCoy, A. J.; Grosse-Kunstleve, R. W.; Adams, P. D.; Winn, M. D.; Storoni, L. C.; Read, R. J., Phaser crystallographic software. *J Appl Crystallogr* **2007,** *40* (Pt 4), 658-674. DOI: 10.1107/S0021889807021206.

(68) Emsley, P.; Lohkamp, B.; Scott, W. G.; Cowtan, K., Features and development of Coot. *Acta Crystallogr D Biol Crystallogr* **2010,** *66* (Pt 4), 486-501. DOI: 10.1107/S0907444910007493.

(69) Afonine, P. V.; Grosse-Kunstleve, R. W.; Echols, N.; Headd, J. J.; Moriarty, N. W.; Mustyakimov, M.; Terwilliger, T. C.; Urzhumtsev, A.; Zwart, P. H.; Adams, P. D., Towards automated crystallographic structure refinement with phenix.refine. *Acta Crystallogr D Biol Crystallogr* **2012,** *68* (Pt 4), 352-67. DOI: 10.1107/S0907444912001308.

(70) Abraham, M. J.; Murtola, T.; Schulz, R.; Páll, S.; Smith, J. C.; Hess, B.; Lindahl, E., GROMACS: High performance molecular simulations through multi-level parallelism from laptops to supercomputers. *SoftwareX* **2015,** *1-2*, 19-25. DOI: 10.1016/j.softx.2015.06.001.

(71) Lindahl, E.; Abraham, M.; Hess, B.; van der Spoel, D. *GROMACS 2020 Reference Manual*, Zenodo: 2020. DOI: 10.5281/zenodo.3562512.

(72) Parrinello, M.; Rahman, A., Polymorphic transitions in single crystals: A new molecular dynamics method. *J Appl Phys* **1981,** *52* (12), 7182-7190. DOI: 10.1063/1.328693.

(73) Páll, S.; Hess, B., A flexible algorithm for calculating pair interactions on SIMD architectures. *Comput Phys Commun* **2013,** *184* (12), 2641-2650. DOI: 10.1016/j.cpc.2013.06.003.

(74) Darden, T.; York, D.; Pedersen, L., Particle mesh Ewald: AnN·log(N) method for Ewald sums in large systems. *J Chem Phys* **1993,** *98* (12), 10089-10092. DOI: 10.1063/1.464397.

(75) Hess, B.; Bekker, H.; Berendsen, H. J. C.; Fraaije, J. G. E. M., LINCS: A linear constraint solver for molecular simulations. *J Comput Chem* **1997,** *18* (12), 1463-1472. DOI: 10.1002/(sici)1096-987x(199709)18:12<1463::Aid-jcc4>3.0.Co;2-h.

(76) Michaud-Agrawal, N.; Denning, E. J.; Woolf, T. B.; Beckstein, O., MDAnalysis: a toolkit for the analysis of molecular dynamics simulations. *J Comput Chem* **2011,** *32* (10), 2319-27. DOI: 10.1002/jcc.21787.

(77) Daura, X.; Gademann, K.; Jaun, B.; Seebach, D.; van Gunsteren, W. F.; Mark, A. E., Peptide Folding: When Simulation Meets Experiment. *Angew Chem Int Ed* **1999,** *38* (1-2), 236-240. DOI: 10.1002/(sici)1521-3773(19990115)38:1/2<236::Aid-anie236>3.0.Co;2-m.

(78) Humphrey, W.; Dalke, A.; Schulten, K., VMD: visual molecular dynamics. *J Mol Graph* **1996,** *14* (1), 33-8, 27-8. DOI: 10.1016/0263-7855(96)00018-5.

TABLES

Table 1. Effect of metal ions on the melting temperature of HfeA.

Treatment	T_m (° C) [a]	ΔT_m
Metal-free	53.85 ± 0.27	-
Mn(II)	71.61 ± 0.12	+ 17.76 [b]
Fe(II)	64.97 ± 0.24	+ 11.12 [b]
Co(II)	76.11 ± 0.20	+ 22.26 [b]
Ni(II)	71.11 ± 0.20	+ 17.26 [b]
Cu(II)	75.07 ± 0.14	+ 21.22 [b]
Zn(II)	78.97 ± 0.58	+ 25.12 [b]

a. Values shown represent the mean ± standard deviation from at least 3 independent measurements.

b. Statistically significant difference to metal-free protein T_m (one-way ANOVA with Tukey post-test).

FIGURE 1

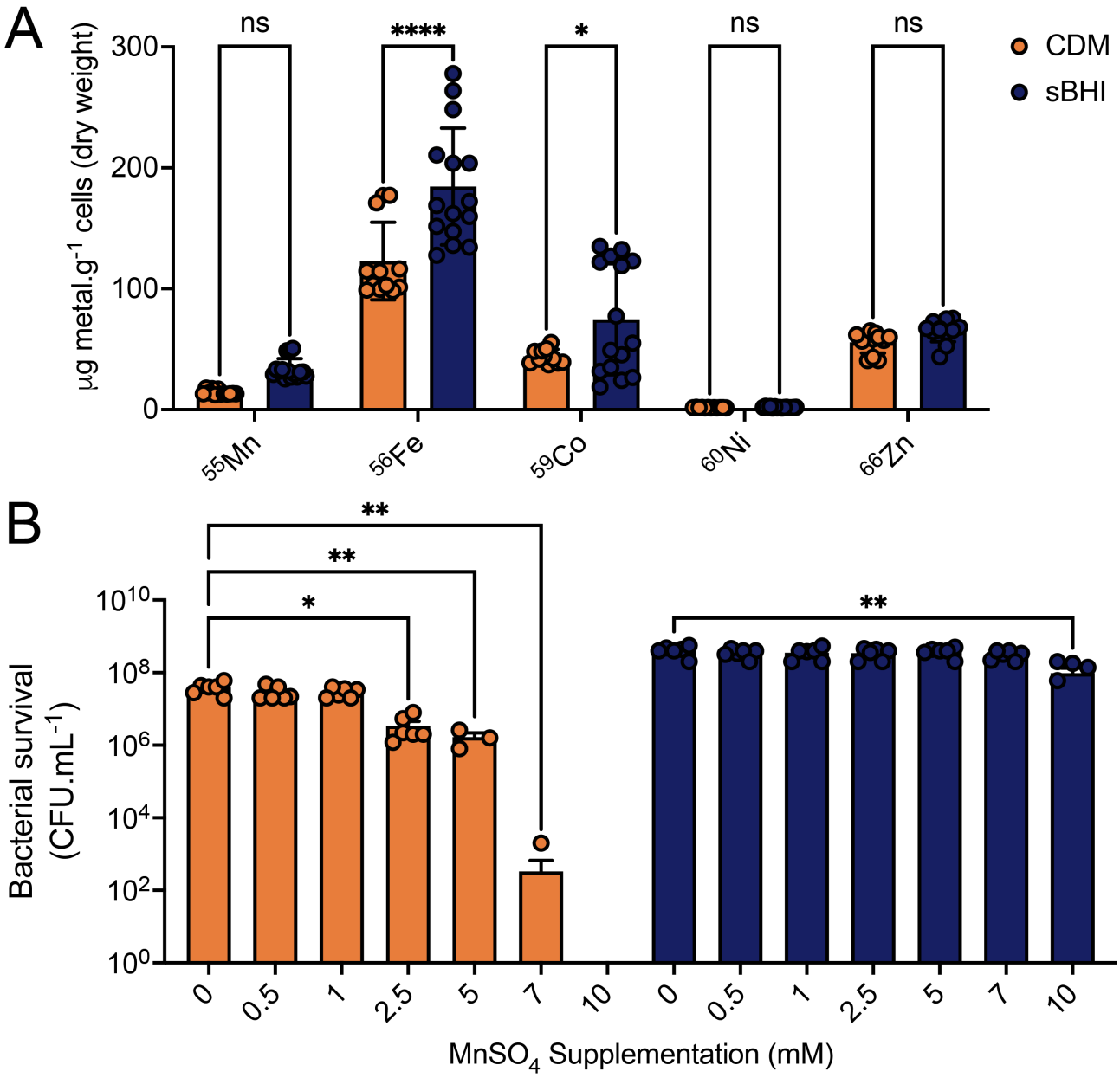

Figure 1. Hi2019 metal accumulation. (**A**) Whole cell accumulation of ^{55}Mn, ^{56}Fe, ^{59}Co, ^{60}Ni, and ^{66}Zn in Hi2019 grown on CDM (orange) or BHI (blue). Data are mean µg metal per g cells (dry weight) (± S.E.M.) from four independent experiments. Statistical significance of the difference determined by two-way ANOVA with Bonferroni post-test; ns, not significant; *, $P < 0.05$; ****, $P < 0.0001$. (**B**) Bacterial survival of Hi2019 in the presence of supra-physiological $MnSO_4$ supplementation in CDM (orange) or BHI (blue). Data represent mean bacterial counts (CFU.mL^{-1} ± S.E.M.) from six independent experiments. Where data points are not visible, no survival was

observed. Statistical significance of the difference determined by a Brown-Forsythe and Welch ANOVA test with Dunnet post-test; *, $P < 0.05$; **, $P < 0.01$.

FIGURE 2

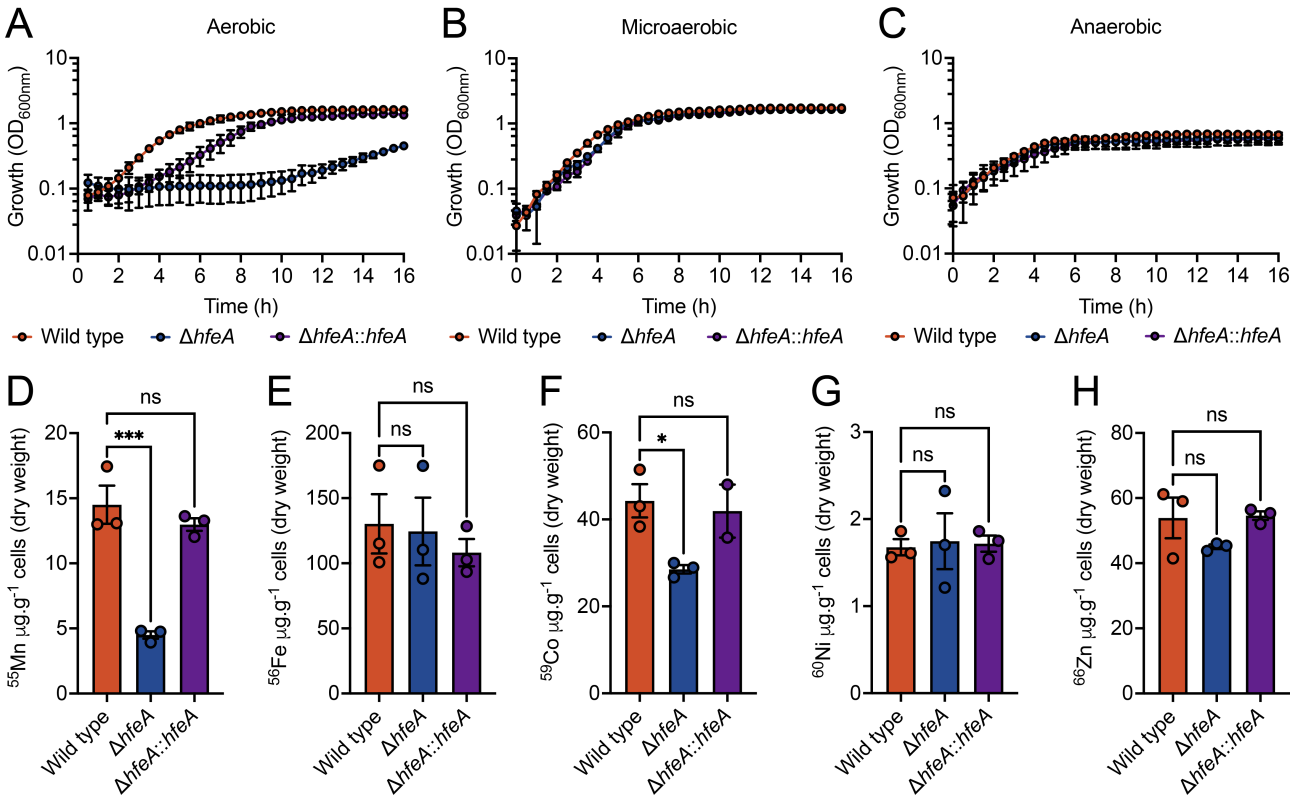

Figure 2. The contribution of *H. influenzae hfeA* to growth and metal uptake. Growth phenotypes of the Hi2019 wild-type, Δ*hfeA*, and complemented strains grown in CDM under (**A**) aerobic, (**B**) microaerobic and (**C**) anaerobic conditions. Data are mean OD_{600} values (± S.E.M.) from three independent biological experiments. Total cellular content of the Hi2019 strains grown in CDM for ^{55}Mn (**D**), ^{56}Fe (**E**), ^{59}Co (**F**), ^{60}Ni (**G**), and ^{66}Zn (**H**), respectively. Data are mean values (± S.E.M.) from three independent biological experiments with statistical significance of the difference determined by one way ANOVA with Tukey post-test; *, $P < 0.05$; ***, $P < 0.001$.

FIGURE 3

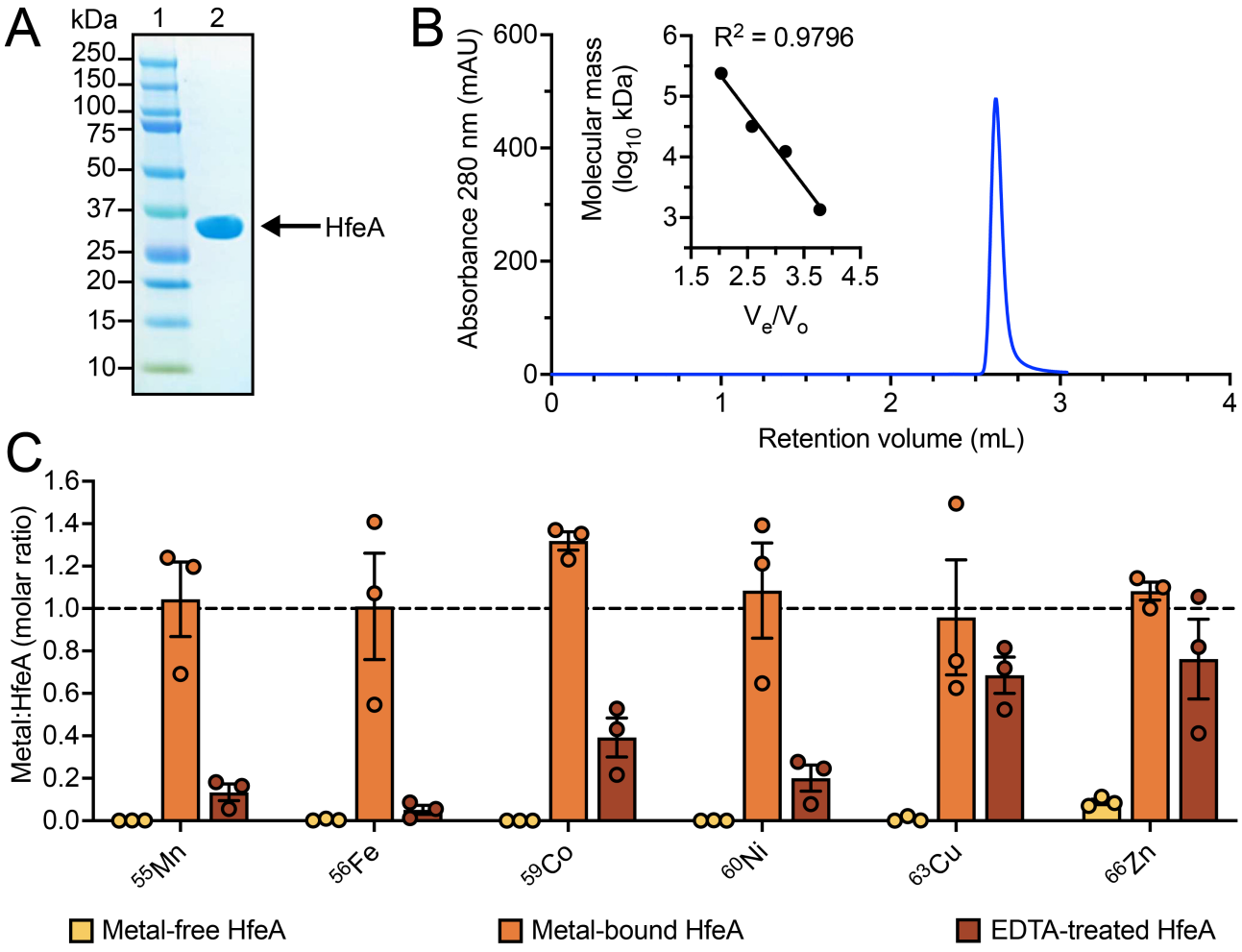

Figure 3. Purification of recombinant wild-type HfeA. (**A**) Coomassie-stained 4-12% Bis-Tris PAGE showing: lane 1, molecular weight standards with sizes indicated (left) and lane 2, recombinant tag-cleaved HfeA. (**B**) Absorbance (280 nm) trace of recombinant HfeA, analyzed by size exclusion chromatography using an Agilent Bio SEC-3 column. The inset represents linear regression of the column calibration using protein molecular weight standards. (**C**) *In vitro* metal-binding experiments of the metal-free, metal-bound, and EDTA-treated (following metal-binding) HfeA with indicated metal ions. Data represent the mean molar ratio of metal ions to HfeA (± S.E.M.) from at least three independent biological experiments.

FIGURE 4

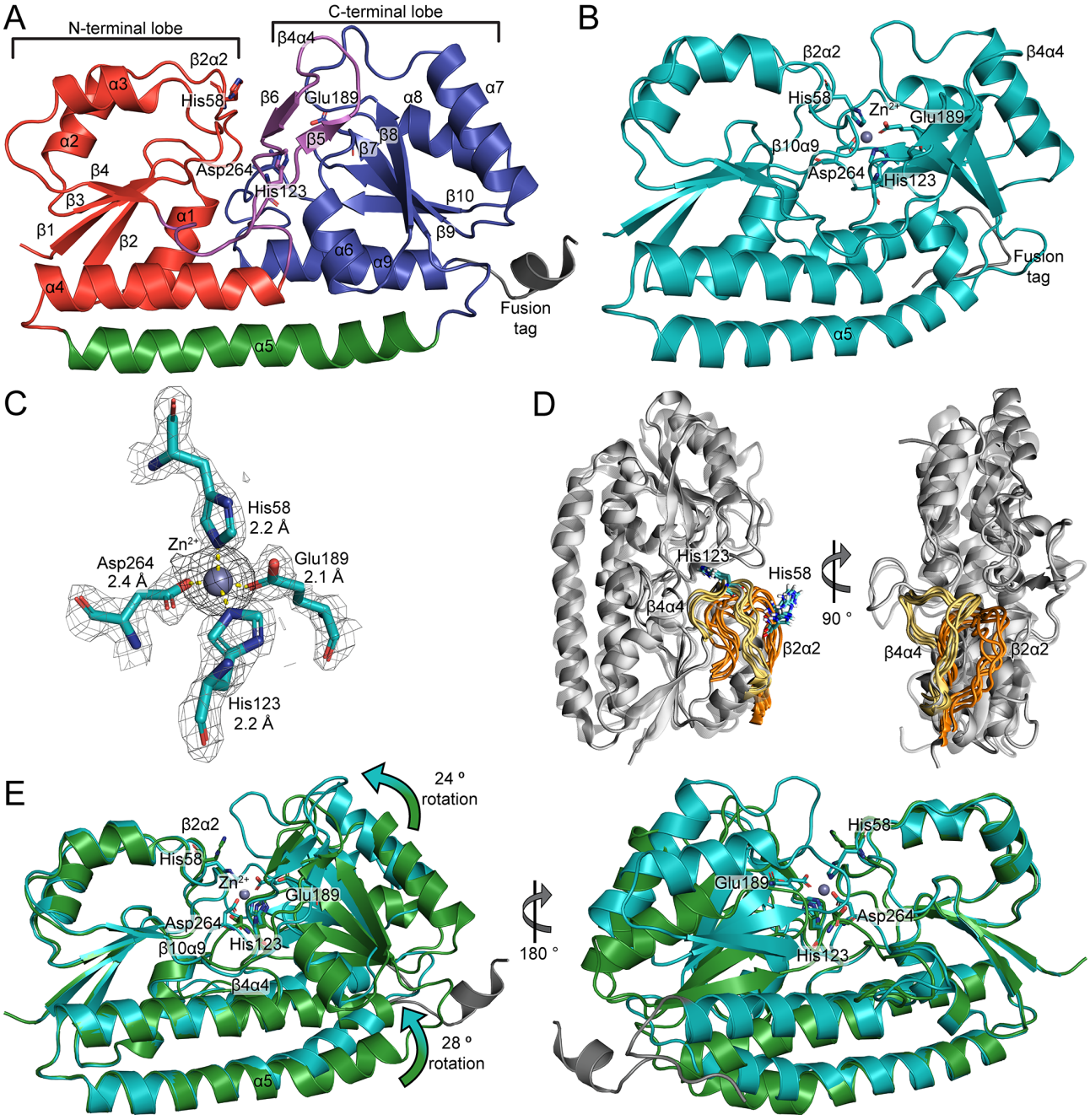

Figure 4. Structural and molecular dynamics simulation analyses of metal-free and Zn(II)-bound Hi2019 HfeA. (**A**) Cartoon representation of metal-free HfeA. N-terminal, C-terminal and the α-helical linker are shown in red, blue, and green, respectively. The long flexible α4β4 loop is shown in magenta. The modelled residues that are part of the fusion tag are shown in grey. The secondary structures of the protein are assigned and labelled. The four residues involved in metal-binding are shown in stick representation. The nitrogen and oxygen atoms are colored blue and red, respectively. (**B**) Cartoon representation of Zn(II)-bound HfeA (teal). The secondary structures of the protein are

assigned and labelled. The four residues involved in metal-binding are shown in stick representation. The Zn(II) metal ion is shown as a grey sphere. The nitrogen and oxygen atoms are colored blue and red, respectively. (**C**) Tetracoordinate hydrogen bonding of Zn(II) metal ion at the binding site. Hydrogen bonds are shown as yellow dotted lines, labelled with respective bond lengths, the metal ion is represented by a sphere, and residues are shown in stick representation. The $2mF_o$-DF_c electron density maps of the coordinating residues and metals are colored in grey and contoured at 1.5 σ, within a 2.0 Å radius around each residue. Polder (OMIT) electron density maps of the metals are colored in black and contoured at 4.0 σ, within a 2.0 Å radius around the ligand. (**D**) MD simulations examining the mobility of the histidine-containing loops. A representative structure of the full-length, reconstructed Hi2019 HfeA structure is shown in grey and overlayed with 4 conformations of loops from the simulations: β2α2, which contains His58, shown in orange; and β4α4, which contains His123, shown in yellow. (**E**) Structural superposition of the crystal structures of metal-free (green) and Zn(II)-bound (teal) HfeA in cartoon representation. Key secondary structures, loops, and residues are assigned and labelled as in (B).

FIGURE 5

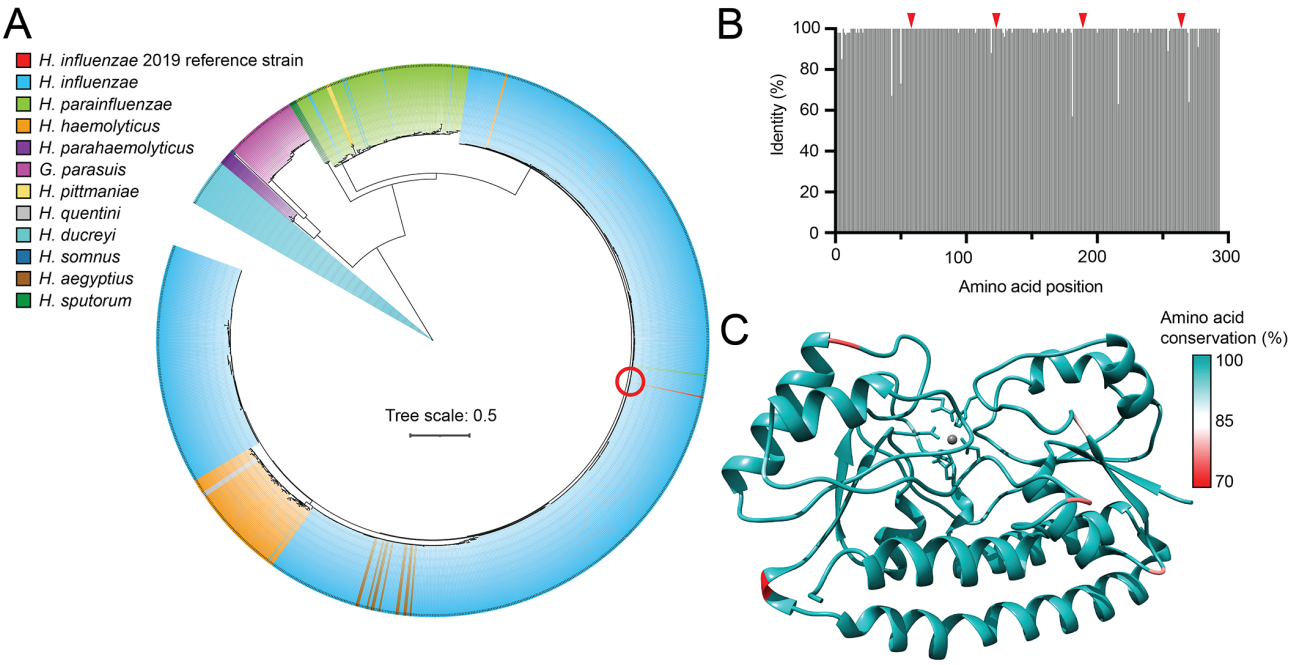

Figure 5. Conservation of the HfeABCD transporter in the *Haemophilus* genus. (A) Phylogenetic analysis of *hfeA* nucleotide sequences from 1,073 publicly available *Haemophilus* spp. genomes. *Influenzae* and non-*influenzae* species are indicated with Hi2019 shown by a red circle. Aligned HfeA amino acid sequences were used to: **(B)** determine the frequency of variation at each position within the protein; and **(C)** map amino acid conservation onto the cartoon-representation of the Zn(II)-bound Hi2019 HfeA crystal structure (7U6T). The fusion tag was excluded from analysis (residues 294-297). The percentage conservation in (C) is shown as a heat map colored from red (70%) to white (85%) to teal (100%). Metal-coordinating residues are represented by sticks (**C**) and red arrows (**B**).

FIGURE 6

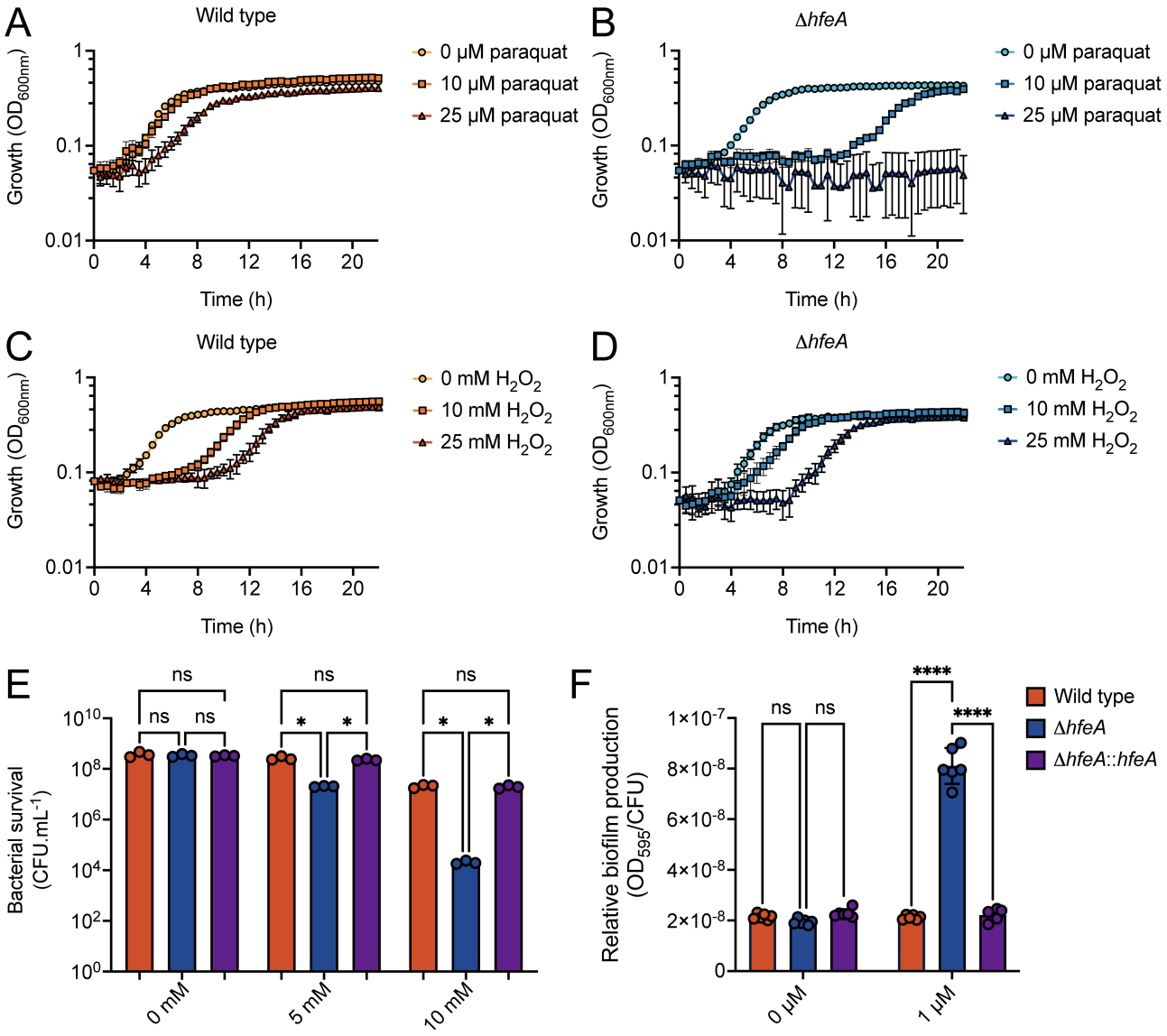

Figure 6. The role of HfeA in stress resistance and biofilm formation. Growth phenotypes of the Hi2019 wild-type (**A, C**) and Δ*hfeA* (**B, D**) strains in the presence of paraquat (A, B) and hydrogen peroxide (C, D). Data are mean OD_{600} values (± S.E.M.) from three independent biological experiments. (**E**) Relative survival of the Hi2019 wild-type, Δ*hfeA*, and complemented strains upon exposure to 0 – 10 mM paraquat. Bacterial survival data are mean CFU mL^{-1} (± S.E.M.) at 1 h from three independent biological experiments. Statistical significance of the difference determined by a Brown-Forsythe and Welch ANOVA with Dunnet post-test; *, $P < 0.05$. (**F**) Relative biofilm production of the Hi2019 strains in response to 1 µM paraquat exposure. Data represents the amount of biofilm produced relative to bacterial density (± S.E.M.) at 16 h from 6 independent experiments.

Statistical significance of the difference determined by a two-way ANOVA with Tukey post-test; ****, $P < 0.0001$.

FIGURE 7

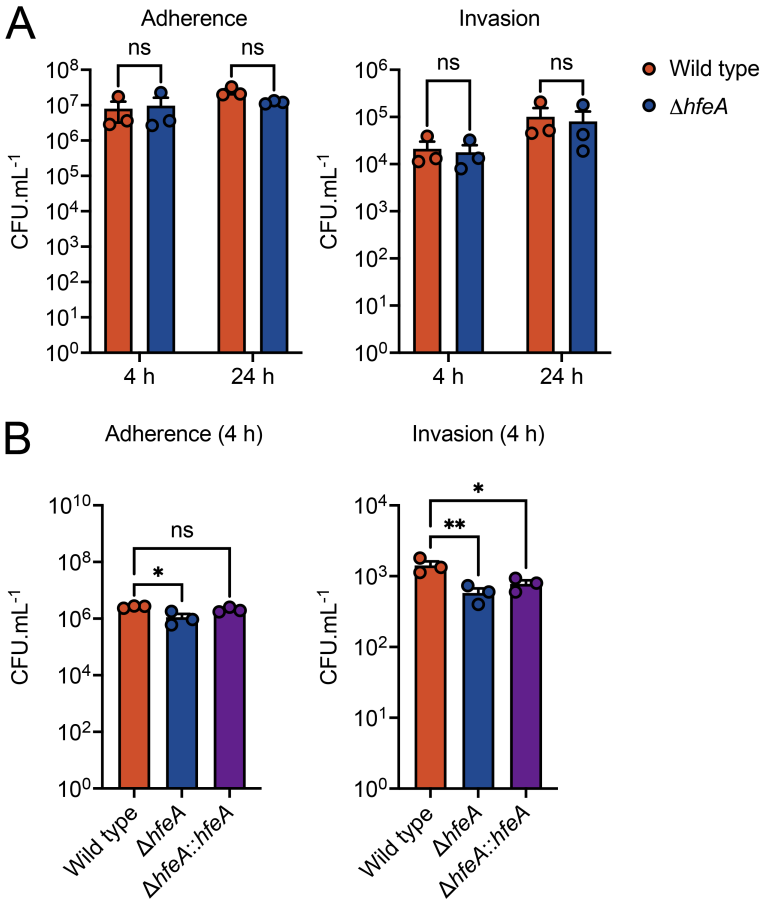

Figure 7. The contribution of HfeA to Hi2019 virulence. (**A**) Interaction of the Hi2019 wild-type and Δ*hfeA* strains with human bronchial epithelial cells (16HBE14) at 4 and 24 h, as measured by adherence and invasion. (**B**) Interaction of the Hi2019 wild-type, Δ*hfeA*, and complemented strains with murine bone marrow macrophages (BMMs) at 4 h, as measured by adherence and invasion. Data represent bacteria recovered, CFU mL^{-1} (± S.E.M.), from 3 independent experiments. Statistical significance of the difference determined by a one-way ANOVA with Tukey post-test; *, $P < 0.05$; **, $P < 0.01$.

For Table of Contents Only

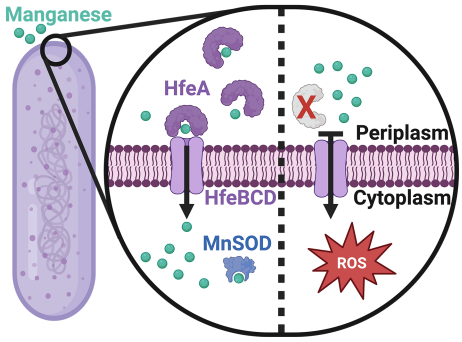

Manuscript title: The Hfe permease and *Haemophilus influenzae* manganese homeostasis

Names of authors: Katherine Ganio, Marufa Nasreen, Zihao Yang, Eve A. Maunders, Zhenyao Luo, Sheikh Imamul Hossain, Dalton H.Y Ngu, Daniel Ellis, Jin Gu, Stephanie L. Neville, Jonathan Wilksch, Adam P. Gunn, Jonathan J. Whittall, Boštjan Kobe, Evelyne Deplazes, Ulrike Kappler, Christopher A. McDevitt.

Brief synopsis: The Gram-negative bacterial pathogen *Haemophilus influenzae* use the manganese-recruiting protein HfeA to import the metal via the HfeBCD transporter into the bacterial cytoplasm. Here, contributes to protection against reactive oxidative species (ROS) stress as a cofactor in the manganese-superoxide dismutase (MnSOD). In a HfeA deficient strain, manganese cannot be transported by this pathway, resulting in loss of MnSOD activity and increased susceptibility to ROS stress.